Simultaneously achieving selective catalytic reduction of NO_x with NH_3 and catalytic oxidation of CO with O_2 over one finely optimized bifunctional catalyst $Mn_2Cu_1Al_1O_x$ at low temperatures

Rongrong Gui [a,b], Jiewen Xiao [a,b], Yanshan Gao [a,b], Yuran Li [c], Tingyu Zhu [c], Qiang Wang [a,b,*]

[a] Beijing Key Lab for Source Control Technology of Water Pollution, College of Environmental Science and Engineering, Beijing Forestry University, Beijing 100083, China
[b] Engineering Research Center for Water Pollution Source Control & Eco-remediation, College of Environmental Science and Engineering, Beijing Forestry University, Beijing 100083, China
[c] Research Center for Process Pollution Control, National Engineering Laboratory for Hydrometallurgical Cleaner Production Technology, Institute of Process Engineering, Chinese Academy of Sciences, Beijing 100190, China

ABSTRACT

For coke oven flue gases, the simultaneous removal of NO_x and CO pollutants is highly demanded but still remains a big challenge. So far there isn't a single efficient catalyst that can simultaneously achieve selective catalytic reduction of NO_x by NH_3 and the catalytic oxidation of CO to CO_2 in the presence of excessive O_2 at low temperatures (180–220 °C). Here, we report a bifunctional catalyst $Mn_2Cu_1Al_1O_x$ that possesses dual active sites and is highly active for both NH_3-SCR and CO oxidation reactions under the above mentioned conditions. By tuning the redox properties and surface oxygen vacancies, the optimized $Mn_2Cu_1Al_1O_x$ catalyst achieved high conversions of both NO_x and CO in the NH_3-NO-CO-O_2 system, with a NO_x conversion of 86.8% and a CO conversion of 100% at 200 °C. The active reaction sites and the interaction principal between NH_3-SCR and CO oxidation reactions were thoroughly investigated by well-designed experiments, in-situ DRIFTS and DFT calculations. It was revealed that NH_3 and CO competed for the same active sites, which significantly influenced the catalytic performance of $Mn_3Al_1O_x$ and $Cu_3Al_1O_x$ for CO oxidation reactions. For the bifunctional $Mn_2Cu_1Al_1O_x$ catalyst, CO is more easily adsorbed on the Cu sites, while NH_3 is more inclined to adsorb on the Mn sites, which enables both NH_3-SCR and CO oxidation reactions to proceed simultaneously on one catalyst. The improvement of CO oxidation performance on $Mn_2Cu_1Al_1O_x$ catalyst is mainly attributed to the reduced Jahn-Teller effect of Cu atoms by doping into Mn_3O_4, which leads to the lift of d-band center and finally enhances the CO adsorption.

1. Introduction

Nitrogen oxides (NO_x) and CO emitted from industrial and commercial combustion processes are environmentally polluting and biologically toxic [1]. For NO_x removal, selective catalytic reduction (SCR) is the most effective and the most widely used technology at present. SCR of NO_x by CO (CO-SCR) has been considered as a feasible way to simultaneously control the NO_x and CO emissions since the first reported by Tauster and Murrell in 1976 [2]. Supported noble metal catalysts have been proven to be effective for CO-SCR, but generally only at high temperature range (250–400 °C) [2–4]. Recent study has revealed Ir catalyst can achieve better deNO$_x$ activity at low temperatures when it is cooperated with other precious metals (e.g. Ru) [5]. Unfortunately,

many studies have noticed that, high concentration of O_2 has a strong inhibitory effect on NO_x abatement for the CO-SCR process while it is inevitable in stationary sources emissions. In the face of more rigorous restrictions on both NO and CO emissions, it is necessary to simultaneously remove these two gas pollutants from stationary sources, particularly for the coke oven flue gases. In 2021, Li et al. [6] reported the first catalyst system Cu–Nb/$Ce_{0.8}Zr_{0.2}O_2$ with dual-function for the simultaneous removal of NO and CO under oxygen-rich conditions. The optimal catalyst 10CuNbCZ presented relatively good NH_3-SCR and CO oxidation activities at 275 °C. Given the fact that the flue gas temperature usually becomes much lower after desulphurizer, a more suitable catalyst that can simultaneously achieve the selective catalytic reduction of NO_x by NH_3 and the catalytic CO oxidation to CO_2 in the presence

of excessive O_2 at low temperatures (< 240 °C) is highly desired.

For the NH_3-SCR process, many transition metal oxides-based catalysts have been developed due to their environmental nontoxicity, moderate price and excellent de-NO_x performance [7–9]. Among them, Mn-based catalysts, such as MnO_x-TiO_2/CeO_2-ZrO_2 [10] and Mn-Fe spinel [11] showed remarkable activities for low-temperature NH_3-SCR reaction, for which the presence of Mn^{4+} species on the catalysts surfaces as well as the high Mn^{4+}/Mn^{3+} ratio were proposed to be critical [10–12]. For CO oxidation, transition metal oxides-based catalysts have also been extensively investigated, which revealed high catalytic activity for CO oxidation to CO_2 as well [13–15]. For example, Luo et al. prepared nanosized CuO-CeO catalyst, with which the T_{90} for CO oxidation could be as low as 80 °C. They demonstrated that the finely dispersed CuO species were the active sites [16]. Being inspired by the above literature reports, we speculated that the well mixed Cu-Mn oxides might be promising for the simultaneously removal of NO_x and CO via the NH_3-SCR as well as the CO oxidation processes.

Layered double hydroxides (LDHs) derived catalysts have attracted great attention for their high activity in various applications. Due to the characteristic structure of LDHs, the obtained layered double oxides (LDOs) catalysts possess favorable properties like high specific surface area, well dispersed active species, as well as the synergistic effects between contained metal elements [17–19]. In this work, a novel bifunctional catalyst $Mn_2Cu_1Al_1O_x$ containing highly dispersed MnO_x active for NH_3-SCR and CuO_x active for CO oxidation was synthesized from MnCuAl-LDH precursor. The highly dispersed Al_2O_3 phase plays an important role as separating and supporting matrix in improving the self-stability of catalyst. The redox properties of this bifunctional catalyst were tuned by optimizing the chemical composition of Cu, Mn and Al elements. The $Mn_2Cu_1Al_1O_x$ catalyst exhibited remarkable activities for both de-NO_x and CO oxidation at a GHSV of 80,000 mL g^{-1} h^{-1}, with a NO_x conversion of 86.8% and a CO conversion of 100% at 200 °C, respectively. The active reaction sites and the interaction between NH_3-SCR and CO oxidation reactions were thoroughly investigated by well-designed experiments and DFT calculations. This contribution represents the first work that can simultaneously achieve NH_3-SCR and CO oxidation reactions in the presence of excessive O_2 over one finely optimized bifunctional catalyst at low temperatures (180–220 °C).

2. Experimental

2.1. Preparation of $Mn_yCu_{3−y}Al_1O_x$ catalysts

The Mn-Cu-Al-NO_3 LDHs were synthesized by a well-recognized aqueous miscible organic solvent treatment (AMOST) method [20]. In the typical procedure, taking $Mn_2Cu_1Al_1$-NO_3 LDH as an example, 50 mL Mn-Cu-Al precursor solution containing 0.025 mol $Mn(NO_3)_2$ aqueous solution (50%), 0.0125 mol $Cu(NO_3)_2$·$3H_2O$ and 0.0125 mol Al $(NO_3)_3$·$9H_2O$ was slowly added to 50 mL anion precursor solution containing 0.025 mol $NaNO_3$. Varied Mn/Cu ratios (2.75:0.25, 2.5:0.5, 2:1, 1.5:1.5) were controlled by adding corresponding amounts of Mn^{2+} and Cu^{2+} in Mn-Cu-Al precursor solution. Since it is difficult to form pure Cu-Al-NO_3 LDH due to the Jahn-Teller effect, Cu-Al-CO_3 LDH was synthesized instead by replacing the above $NaNO_3$ with Na_2CO_3 solution. During the synthesis, the pH was kept constant at 10 by adding suitable amounts of 4 M NaOH solution. In order to prevent the oxidation of Mn^{2+}, the whole aging process was performed under N_2 atmosphere by sealing the round-bottom flask tightly after bubbling with N_2 for at least 10 min. The resulting suspension was aged at room temperature (RT) with vigorous magnetic stirring for 12 h, and then filtered, washed with deionized water until pH = 7 and further rinsed with ethanol thoroughly. Then the ethanol washed solids were redispersed in ethanol and then stirred at RT for another 2 h. The product was finally collected by filtration and dried overnight in an oven at 60 °C. Mixed oxides were formed after calcined at 400 °C for 5 h in air, denoted as $Mn_3Al_1O_x$, $Mn_{2.75}Cu_{0.25}Al_1O_x$, $Mn_{2.5}Cu_{0.5}Al_1O_x$, $Mn_2Cu_1Al_1O_x$,

$Mn_{1.5}Cu_{1.5}Al_1O_x$ and $Cu_3Al_1O_x$, according to the Mn/Cu ratios. For comparison, the Mn-Cu/γ-Al_2O_3 (the total loading of Mn and Cu was 8 wt%, the molar ratio of Mn/Cu = 2:1) catalyst was prepared by a conventional incipient wetness impregnation method.

2.2. Characterization of catalysts

The X-ray diffraction (XRD) analysis of samples was performed on a Shimadzu XRD-7000 diffractometer with Cu K_α radiation. The operating range for 2θ was from 5° to 75° with scanning rate of 5 °C min^{-1} and the step size was 0.02°. The specific surface areas of samples were measured by Builder SSA-7000 instrument via the BET method. The X-ray photoelectron spectroscopy (XPS) was conducted on a Thermo escalab 250Xi equipment with monochromatic Al Kα (1486.6 eV) radiation. The morphologies of samples were observed by scanning electron microscope (SEM, SU-8010, Hitachi) and high resolution transmission electron microscopy (HR-TEM, JEM-2100F, JEOL) with an accelerating voltage of 200 kV. Cu K edge x-ray absorption fine structure (XAFS) of $Mn_2Cu_1Al_1O_x$ and reference materials of Cu foil, Cu_2O and CuO were tested at the beam lines 4B9A of Beijing Synchrotron radiation facility (BSRF). X-ray absorption near-edge spectra (XANES) and extended x-ray absorption fine structure (EXAFS) spectra were analyzed by Athena [21]. The content of the metals (wt%) for the prepared catalysts were measured by inductively coupled plasma optical emission spectrometer (ICP-OES, Agilent ICPOES730).

Temperature-programmed desorption and reduction analyses were tested in a tube furnace equipped with a thermal conductivity detector (TCD). In O_2-TPD measurements, 100 mg of samples were packed in a quartz tube reactor and placed in a tubular furnace. The O_2 adsorption was carried out by flowing 5% O_2/Ar mixture at 50 mL min^{-1} total flow at 50 °C for 30 min, followed by cooling down to RT in Ar flow. The TCD curve was recorded as the temperature rose from RT to 800 °C with a heating rate of 10 °C min^{-1}. NH_3-TPD measurements taken pure NH_3 as the adsorbate, and the adsorption time was 15 min with a flow rate of 30 mL min^{-1} at 80 °C. CO- TPD employed 5% CO/Ar as adsorbate, and the adsorption time lasted for 1 h at 50 °C, followed by purging in Ar for 1 h. The desorption behavior was recorded by a QGA (Hiden Analytical, HAS 301) via the (m/z) signals of Ar (40), CO (28), and CO_2 (44). In H_2-TPR measurements, 5% H_2/Ar flow was passed through the catalyst bed (100 mg) at a flow rate of 30 mL min^{-1}, while the temperature was ramped from RT to 800 °C. All samples were pretreated in an Ar flow at 400 °C for 30 min to clean the catalysts surface before each test.

In-situ diffuse reflectance infrared transform spectroscopy (DRIFTS) measurements were performed using a Fourier transform infrared spectrometer (FT-IR, Spectrum 3, Perkin Elmer), equipped with a liquid N_2 cooled MCT detector. The in situ diffuse-reflectance FTIR measurements were performed in a sealed high-temperature cell fitted with ZnSe windows. Experimental temperature was controlled by a heater and condensate water equipment. Approximately 5 mg of finely ground catalyst was placed in an aluminum crucible and mounted on a commercial in-situ DRIFTS cell (Selector, Specac). Prior to each experiment, the catalyst was heated to 400 °C under N_2 with a total flow rate of 50 mL min^{-1} for 30 min to remove any adsorbed gas or H_2O on the surface of samples. After 30 min, the temperature was then cooled down to 160 °C and the background was collected. The IR spectra were recorded in different gas mixture flow by accumulating appropriate scans (15 s scans for the first 5 min and 128 s scans for the remaining 25 min) at a resolution of 4 cm^{-1} from 700 to 4000 cm^{-1}.

2.3. Density functional theory (DFT) calculation

Density Functional Theory (DFT) calculations were conducted via Vienna Ab Initio Simulation Package (VASP) program, using the Perdew–Burke–Ernzerhof (PBE) functional to describe the electron exchange and correlation. The projector augmented wave (PAW) method was employed to interpret the effect of atomic cores on valence electrons

[22,23]. According to the XRD results (Section 3.1), CuO (C2/c) and Mn$_3$O$_4$ (I41/amd) were chose to build crystal models. The most abundant facets of CuO and Mn$_3$O$_4$ are (111) and (211), respectively. CuO model is a (2 × 1) cell containing 3 layers and 48 units of per slab (a (2 × 1) unit cell, 11.75 × 13.13 Å), and the Mn$_3$O$_4$ is a (1 × 1) cell containing 6 layers and 12 units of TiO$_2$ per slab (a (1 × 1) unit cell, 12.69 × 11.25 Å). The kinetic energy cutoff was 450 eV and each optimized model was separated by 15 Å of vacuum. In geometry optimizations, the uppermost two or four layers were relaxed (with the SCF tolerance of 10^{-6} eV, and atomic forces were converged below 0.02 eV/Å) and the rest was fixed. The spin polarization has been corrected. The Hubbard corrections (DFT+U) of Mn and Cu were U_{eff} = 2.8 (U = 4.0 eV, J = 1.2 eV) and U_{eff} = 4.0 eV (U = 4.0 eV, J = 0 eV), respectively. Due to the large size of the slab (~ 12 Å × 10 Å), the Brillouin zone was integrated using a 2 × 2 × 1 Monkhorst–Pack grid (k-points). The DFT-D3 correction was implemented.

Since the Cu atoms on the surface of CuO(111) was tri-coordinated, the tri-coordinated Mn$_{3c}$ on Mn$_3$O$_4$(211) was selected to be substituted by Cu to simulate the doping condition (denoted by Cu-Mn$_3$O$_4$(211)). In all surface models, the active low-coordinated sites (such as Mn$_{3c}$ and Cu$_{3c}$) were considered as adsorption sites for CO or NH$_3$ molecules. The adsorption energy of CO and NH$_3$ defined as E_{ads} was calculated as follows [24]:

$$E_{ads} = E_{CO/NH_3+surface} - (E_{surface} + \quad E_{CO/NH_3}) \tag{1}$$

where $E_{CO/NH_3+surface}$ is the total energy of the CO or NH$_3$ molecule absorbed on the surface, $E_{surface}$ is the total energy of the surface and E_{CO/NH_3} is the energy of isolated CO or NH$_3$ molecule in the vacuum.

The charge density difference was defined by Eq. (2):

$$\Delta\rho = \rho_{mol/sur} - \rho_{mol} - \rho_{sur} \tag{2}$$

where $\rho_{mol/sur}$, ρ_{mol} and ρ_{sur} are the electron densities of the molecule adsorbed on the surface, of the individual electron density of molecule, and of the surface, respectively.

The d band center was calculated by Eq. (3):

$$\varepsilon_d^c = \frac{\int_{-\infty}^{E_f} E\rho_d(E)dE}{\int_{-\infty}^{E_f} \rho_d(E)dE} \tag{3}$$

where E is the Energy, E_f is the Fermi level and ρ_d is the density of states (DOS).

2.4. Catalytic activity tests

The catalytic activities of catalysts were tested in a fixed-bed stainless steel reactor with an internal diameter of 10 mm at atmospheric pressure, equipped with a temperature programmed controller. The reaction conditions were as follows: 500 ppm NO, 500 ppm NH$_3$, 5000 ppm CO, 5 vol% O$_2$, 5% H$_2$O (when used), 50 ppm SO$_2$ (when used) and Ar as balance with a total gas flow rate of 200 mL min^{-1}, corresponding to a GHSV of 80,000 mL g^{-1} h^{-1}. The outlet concentration of NO, NO$_2$, N$_2$O, NH$_3$ and CO in the flue gas was quantitated by a MKS-2000 FTIR spectrometer. The NO$_x$ (NO and NO$_2$) conversion rate, CO conversion rate, and N$_2$ selectivity were calculated using Eqs. (4)–(6).

$$NO_x \text{ conversion}(\%) = \left(1 - \frac{NO_{x(out)}}{NO_{x(in)}}\right) \times 100\% \tag{4}$$

$$CO \text{ conversion}(\%) = \left(1 - \frac{CO_{(out)}}{CO_{(in)}}\right) \times 100\% \tag{5}$$

$$N_2 \text{ selectivity}(\%) = \left(1 - \frac{2N_2O_{(out)}}{(NO_{x(in)} - NO_{x(out)}) + (NH_{3(in)} - NH_{3(out)})}\right) \times 100\% \tag{6}$$

where NO$_x$(CO)$_{(in)}$ and NO$_x$(CO)$_{(out)}$ are the concentration of NO$_x$(CO) in the gas flow before and after the catalysts bed, respectively.

The reaction rate normalized by the specific surface area and the turnover frequency (TOF) of the catalysts employed were calculated by Eqs. (7) and (8).

$$\text{reaction rate (mmol m}^{-2}\text{ h}^{-1}) = \frac{C_{NO_x(CO)} \times x_{NO_x(CO)} \times V}{V_m \times W \times S_{BET}} \tag{7}$$

$$\text{TOF }(s^{-1}) = \frac{C_{NO_x(CO)} \times x_{NO_x(CO)} \times V}{V_m \times n_{Mn(Cu)}} \tag{8}$$

where $C_{NO_x(CO)}$ is the concentration of NO$_x$(CO) (ppm), $x_{NO_x(CO)}$ is the conversion (%) of NO$_x$(CO), V is the volumetric flow rate (mL s^{-1}), V_m is the molar volume of gas (22.4 L mol^{-1}), W is the weight of the catalyst (g), S_{BET} is the specific surface area of the catalyst (m^2 g^{-1}), $n_{Mn(Cu)}$ is the total amount of Mn(Cu) atoms (mol), estimated by the results of XPS and ICP–MS. The conversion rate (%) of NO$_x$(CO) of the selected samples was controlled below 20% at selected reaction temperatures (120–180 °C) by adjusting the GHSV to 40,000–120,000 mL g^{-1} h^{-1} to eliminate the influence of diffusion. The apparent activation energy (Ea, kJ mol^{-1}) was calculated from the slope of the Arrhenius plot according to Eqs. (9) and (10).

$$\ln k = -\frac{E_a}{RT} + \ln A \tag{9}$$

$$k = -\frac{V}{W} \times \ln(1 - x) \tag{10}$$

where k is the reaction rate constant (mL g^{-1} s^{-1}), A is the pre-exponential factor (mL g^{-1} s^{-1}), R is the standard gas constant (J mol^{-1} K^{-1}), T is the reaction temperature (K), W is the catalyst weight (g), V is the volumetric flow rate (mL s^{-1}) and x is the conversion rate (maintained below 20%).

3. Results and discussion

3.1. Structural and textural characterization of catalysts

The crystal structures of synthesized LDHs precursors and the derived LDO catalysts after calcination were first identified using XRD analyses. As illustrated in Fig. 1a, four LDH precursors with different Mn/Cu ratios all exhibited the characteristic diffraction peaks of LDHs structure. The diffraction peaks at 2θ = 10.1°, 20.6° and 33.6° can be attributed to the reflections of (*003*), (*006*), and (*012*) planes for Mn$_x$Cu$_{3-x}$Al$_1$-NO$_3$ LDHs phase, respectively [19]. Comparing to the NO$_3^-$ intercalated LDHs, the position of characteristic (*00l*) diffraction peaks of Cu$_3$Al$_1$-CO$_3$ LDH moved slightly to higher values due to the difference between the guest anions CO$_3^{2-}$ and NO$_3^-$ in dimension and carried charges, which further led to the variation of basal spacing values (d$_{003}$) [25]. After being calcined at 400 °C, the layered structure of LDHs was collapsed because of the escape of the interlayer anions and water molecules and the decomposition of hydroxyl groups, consequently forming well mixed metal oxides. In Fig. 1b, the diffraction peaks at 2θ = 18.0°, 29.0°, 32.4°, 35.9°, and 60.0° confirmed the formation of Hausmannite Mn$_3$O$_4$ (JCPDS no. 24-0734) in Mn$_3$Al$_1$O$_x$, while the diffraction peaks at 2θ = 35.6° and 38.8° could be ascribed to CuO
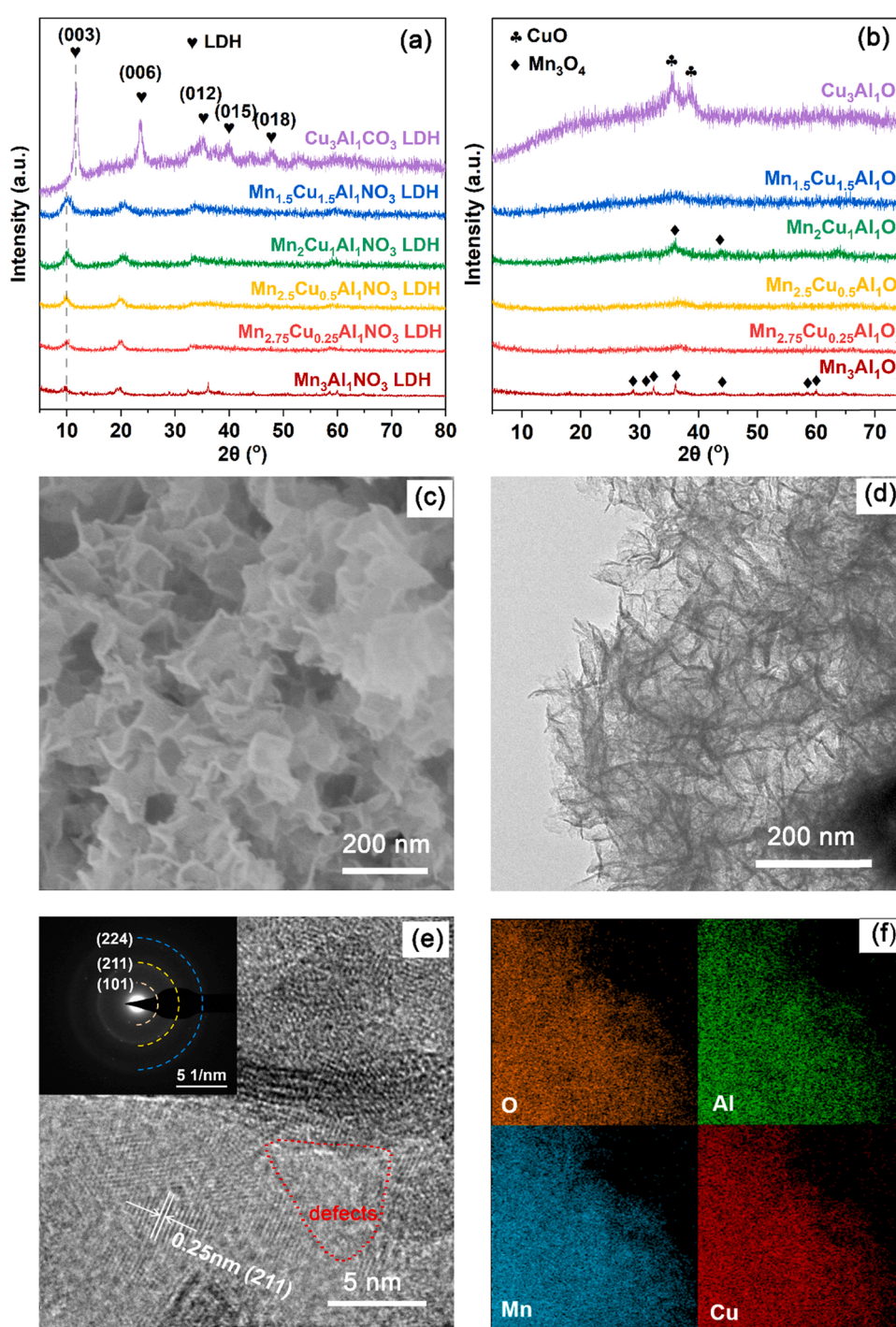
Fig. 1. XRD patterns of (a) $Mn_xCu_{3-x}Al_1$-NO_3 LDHs, (b) $Mn_yCu_{3-y}Al_1O_x$ LDOs with different Mn/Cu ratios, (c) SEM image, (d) TEM image, (e) HR-TEM image and (f) elemental mapping analysis of the $Mn_2Cu_1Al_1O_x$ catalyst.

(JCPDS no. 48-1548) in $Cu_3Al_1O_x$. For $Mn_yCu_{3-y}Al_1O_x$ samples, the CuO phase was not detected, and the broad low-intensity peaks located at 35.9° might indicate the distortion of Mn_3O_4 lattice caused by the introduction of Cu.

The morphology and textural properties of synthesized samples were further observed by SEM and TEM analyses. The $Mn_2Cu_1Al_1O_x$ LDO showed a typical "flower-like" morphology, consisting of thin nano-flakes with irregular stacking and arrangement (Fig. 1c, d). In Fig. 1e, the crystalline lattice with the same interplanar spacing of 0.25 nm, along with the inserted selected area electron diffraction (SAED) pattern confirm the crystal (211) plane of Mn_3O_4. The amorphous area

suggested the formation of the lattice distortion and abundant defects. Fig. 1f depicts TEM–EDX mapping of $Mn_2Cu_1Al_1O_x$ sample. Manganese, copper, aluminum and oxygen were homogeneously distributed in $Mn_2Cu_1Al_1O_x$, indicating both Cu and Mn oxides were in highly dispersed states. Njagi et al. have synthesized copper manganese oxides with high CO oxidation activity using a novel redox method [13]. They believed that the improvement of catalytic activity was closely related to the nanocrystalline and homogeneous properties of the catalyst. Table 1 summarizes the BET specific surface area, pore volume, and pore size of all catalysts prepared in this work. Compared with the $Mn_3Al_1O_x$, $Cu_3Al_1O_x$ and Mn-Cu/γ-Al_2O_3 catalyst, $Mn_yCu_{3-y}Al_1O_x$ series catalysts

Table 1

The BET specific surface area, pore volume, and pore size of synthesized $Mn_{1.5}Cu_{1.5}Al_1O_x$, $Mn_2Cu_1Al_1O_x$, $Mn_{2.5}Cu_{0.5}Al_1O_x$, $Mn_{2.75}Cu_{0.25}Al_1O_x$, $Mn_3Al_1O_x$, $Cu_3Al_1O_x$, and Mn-Cu/γ-Al$_2$O$_3$ catalysts.

Catalysts	BET specific surface area (m^2 g^{-1})	Pore Volume (cm^3 g^{-1})	Pore size (Å)
$Mn_{1.5}Cu_{1.5}Al_1O_x$	236.7	1.29	109.3
$Mn_2Cu_1Al_1O_x$	206.8	1.34	129.9
$Mn_{2.5}Cu_{0.5}Al_1O_x$	192.4	1.18	122.3
$Mn_{2.75}Cu_{0.25}Al_1O_x$	186.3	1.21	129.8
$Mn_3Al_1O_x$	150.1	1.07	143.2
$Cu_3Al_1O_x$	94.9	0.91	191.8
Mn-Cu/γ-Al$_2$O$_3$	144	0.36	49.9

possessed higher specific surface area and pore volume. Both the highly dispersed active species and the higher specific surface area are favorable for the adsorption of the gas reactants and facilitate the chemical reaction processes. The above analysis of the texture properties of the $Mn_2Cu_1Al_1O_x$ sample proves its porous, defect-rich, small grain, larger surface area features.

3.2. Catalytic performance of catalysts

The catalytic performance of synthesized $Mn_3Al_1O_x$, $Cu_3Al_1O_x$, $Mn_yCu_{3-y}Al_1O_x$, and Mn-Cu/γ-Al$_2$O$_3$ catalysts were comparatively investigated for neat NH$_3$-SCR reaction (NH$_3$-NO-O$_2$ system), neat CO oxidation reaction (CO-O$_2$ system), and co-occurrence of both NH$_3$-SCR and CO oxidation reactions (NH$_3$-NO-CO-O$_2$ system) in the temperature range of 120–300 °C. We particularly paid much attention on the interaction effect between NH$_3$-SCR and CO oxidation reactions, for instance, will one reaction influence the other when they occurred simultaneously on the same catalyst. The purpose is to develop a new catalyst that can simultaneously achieve both NH$_3$-SCR and CO oxidation reactions efficiently, resulting high conversions of both NO$_x$ and CO in the NH$_3$-NO-CO-O$_2$ system at low temperatures (< 240 °C).

Fig. 2a, b indicate that $Mn_3Al_1O_x$ shows excellent NH$_3$-SCR activity but low CO oxidation activity whether tested separately or not. For neat NH$_3$-SCR reaction, the NO$_x$ conversion rate reached 81.4% at 200 °C, and the addition of 5000 ppm CO had a little effect on NO$_x$ conversion over $Mn_3Al_1O_x$ catalyst (Fig. 2a). For neat CO oxidation reaction, the CO conversion rate was very low (< 40%) at temperatures 100–240 °C, and the addition of 500 ppm NH$_3$ and 500 ppm NO slightly increased the CO conversion over $Mn_3Al_1O_x$ catalyst (Fig. 2b). These results suggested the $Mn_3Al_1O_x$ catalyst could not simultaneously achieve both NH$_3$-SCR and CO oxidation reactions efficiently in the low temperature range (120–240 °C).

Fig. 2c shows $Cu_3Al_1O_x$ catalyst is not active for neat NH$_3$-SCR reaction, with the NO$_x$ conversion below 20% in the whole temperature range, and the addition of 5000 ppm CO has little effect on NO$_x$ conversion. Fig. 2d indicates $Cu_3Al_1O_x$ catalyst obtained a CO conversion rate of 95.3% at 300 °C, but the addition of 500 ppm NH$_3$ and 500 ppm NO decreased the CO conversion to a certain extent. Compared to $Mn_3Al_1O_x$ catalyst, $Cu_3Al_1O_x$ catalyst exhibited a better CO oxidation activity, the CO conversion rate was 8.4% for the former but 58.8% for the later at 200 °C. These results suggested $Cu_3Al_1O_x$ catalyst could not simultaneously achieve both NH$_3$-SCR and CO oxidation reactions efficiently neither.

The above results suggested MnO$_x$ is relatively better for NH$_3$-SCR reaction and CuO$_x$ is relatively more active for CO oxidation, which inspired us to design a novel bifunctional catalyst containing both highly dispersed MnO$_x$ and CuO$_x$ species. By tuning the Mn/Cu ratio, we presume it is highly possible to achieve high conversions of both NO$_x$ and CO in the NH$_3$-NO-CO-O$_2$ system over one optimized catalyst at low temperatures. Therefore, the catalytic performance of a series of LDH-derived $Mn_yCu_{3-y}Al_1O_x$ catalysts with different Mn/Cu ratios in the NH$_3$-NO-CO-O$_2$ system was evaluated in the temperature range of

120–300 °C. For comparison purpose, Mn-Cu/γ-Al$_2$O$_3$ catalyst was also studied as a control catalyst.

Fig. 2e, f indicate the $Mn_yCu_{3-y}Al_1O_x$ catalysts possess superior de-NO$_x$ and CO oxidation activity, compared to the conventional Mn-Cu/γ-Al$_2$O$_3$ catalysts. Apparently, the NO$_x$ conversion increased with the increase of Mn content (Fig. 2e), while the CO conversion increased with the increase of Cu content (Fig. 2f). It is considered that the selectivity of CO conversion to CO$_2$ is 100% since only CO$_2$ was detected in the outlet gas, while other components, such as CH$_4$ and HCNO, were not detected. Among all catalysts, $Mn_2Cu_1Al_1O_x$ achieved the best catalytic performance for the simultaneous removal of NO$_x$ and CO, with a conversion rate of 86.8% and 100% for NO$_x$ and CO at 200 °C, respectively. The N$_2$ selectivity shown in Fig. S1 decreased with the elevation of temperature for all catalysts, which was due to the N$_2$O formation via NH$_3$ oxidation and undesired SCR process. The result revealed the LDH-derived $Mn_yCu_{3-y}Al_1O_x$ catalysts can achieve high conversions of both NO$_x$ and CO in the NH$_3$-NO-CO-O$_2$ system. By contrast, the performance of Mn-Cu/γ-Al$_2$O$_3$ catalyst obtained by a conventional impregnation method was much worse. To the best of our knowledge, the LDH-derived $Mn_2Cu_1Al_1O_x$ represents the very first bifunctional catalyst can simultaneously achieve both NH$_3$-SCR and CO oxidation reactions efficiently at low temperatures (180–220 °C), with high conversions of both NO$_x$ and CO in the NH$_3$-NO-CO-O$_2$ system.

The SO$_2$ tolerance of $Mn_2Cu_1Al_1O_x$ and $Mn_3Al_1O_x$ catalysts was then evaluated in the presence of allowable SO$_2$ concentration (50 ppm) for 6 h. After introducing 50 ppm SO$_2$ into the flow gas, the conversion rates of NO$_x$ and CO both declined with time due to the deposition of sulfates on the surface of catalysts (Fig. S2). The NO$_x$ conversion decreased by ∼ 10.4% for $Mn_2Cu_1Al_1O_x$ but ∼ 18.1% for $Mn_3Al_1O_x$ after 6 h of exposure to 50 ppm SO$_2$. The CO conversion of $Mn_2Cu_1Al_1O_x$ was maintained at 100% within 6 h, while it decreased by 88.3% for $Mn_3Al_1O_x$. In all, it can be concluded that the $Mn_2Cu_1Al_1O_x$ catalyst possesses better SO$_2$ resistance.

CO is also a possible reducing agent for NO$_x$ reduction, in addition to NH$_3$, in the NH$_3$-NO-CO-O$_2$ system. Therefore, the performance of $Mn_2Cu_1Al_1O_x$ catalysts for CO-SCR reaction was tested in the presence and absence of O$_2$. As shown in Fig. 3, in O$_2$-rich atmosphere, CO-SCR reaction activity was always very low, which meant that it contributed little to N$_2$ generation in the NH$_3$-NO-CO-O$_2$ system. When excess O$_2$ existed, CO was always preferentially oxidized by O$_2$ rather than NO, which led to a number of CO-SCR studies under O$_2$-free conditions [5]. It is interesting to note that in the NH$_3$-NO-CO system, a considerable portion of NO was converted to NH$_3$ once the temperature was over 200 °C. It is speculated that this is related to the hydroxylation of catalyst surface and water-gas shift reaction in wet environment.

The reaction rates of NO$_x$ and CO conversions normalized by the specific surface area of employed catalysts were calculated to evaluate the conversion efficiency of the active sites for NH$_3$-SCR and CO oxidation reactions over $Mn_2Cu_1Al_1O_x$, $Mn_3Al_1O_x$, and $Cu_3Al_1O_x$ catalysts (Table 2). For $Mn_2Cu_1Al_1O_x$, the NO$_x$ reaction rates were lower than those of $Mn_3Al_1O_x$, which is consistent with the experimental results (120–180 °C, Fig. 2). In contrast, the CO reaction rate for $Mn_2Cu_1Al_1O_x$ was significantly higher than that for $Mn_3Al_1O_x$ and $Cu_3Al_1O_x$ catalysts, indicating the remarkable enhanced CO removal efficiency by the introduction of Cu when NH$_3$-SCR reaction occurred at the same time. These results are consistent with the trend indicated by the estimated TOF values listed in Table S1. It should be noted that the calculations were based on the assumption that these two simultaneous reactions occurred separately on different active sites on $Mn_2Cu_1Al_1O_x$ catalysts, that is, Mn^{4+} served as the active sites for NH$_3$-SCR reaction and Cu$^+$ for CO oxidation, and the competition between these two simultaneous reactions at the single active sites contained catalysts, ie. $Mn_3Al_1O_x$ and $Cu_3Al_1O_x$ catalysts, was ignored. Fig. S3 illustrates the Arrhenius plots of NH$_3$-SCR and CO oxidation reaction rates over the above catalysts studied. By comparing the Ea values for $Mn_2Cu_1Al_1O_x$ and $Mn_3Al_1O_x$, it can be seen that the activation energy of NH$_3$-SCR
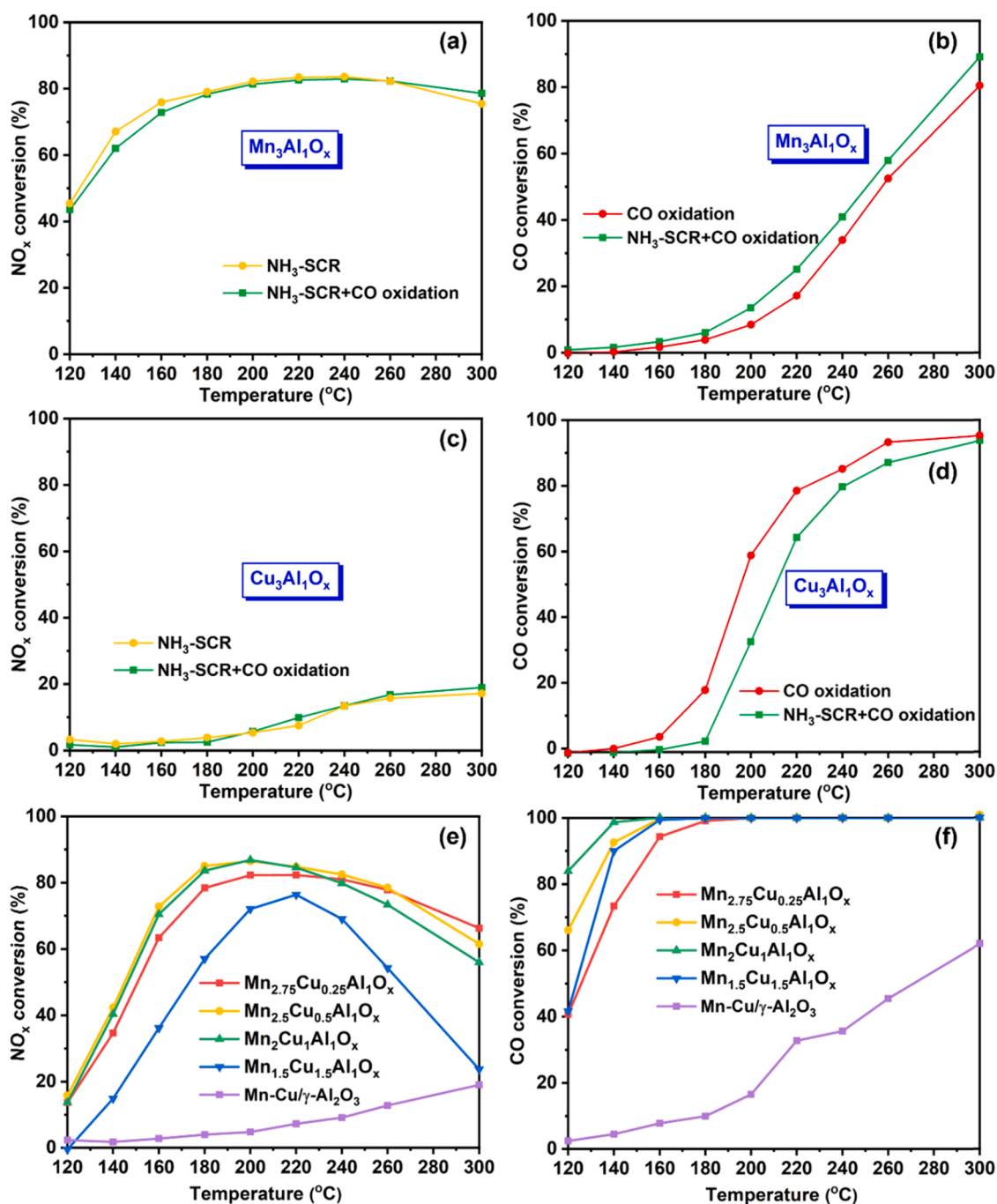
Fig. 2. The influence of different atmosphere on the activity of $Mn_3Al_1O_x$ (a) NO_x conversion, (b) CO conversion, $Cu_3Al_1O_x$ (c) NO_x conversion, (d) CO conversion and the influence of Mn/Cu ratio on the activity of $Mn_yCu_{3-y}Al_1O_x$ mixed oxide catalysts and Mn-Cu/γ-Al_2O_3 catalyst under the NH_3-SCR + CO oxidation atmosphere: (e) NO_x conversion, (f) CO conversion in the presence of water. Reaction conditions: $[NO_x]$ = $[NH_3]$ = 500 ppm (when used), [CO] = 5000 ppm (when used), $[O_2]$ = 5%, $[H_2O]$ = ~ 5%, balance Ar, total flow rate = 200 mL min^{-1}, operating temperature = 120–300 °C, catalyst 0.15 g.

reactions does not change significantly, while the varied reaction rates suggests a difference in the number of active sites [15]. For CO oxidation, the introduction of Cu in $Mn_2Cu_1Al_1O_x$ induced a different type of active sites, resulting in a lower energy barrier and higher reaction rates (120–180 °C).

3.3. Redox properties and oxygen vacancies of catalysts

XPS is an effective technology to analyze the surface chemical properties and metal valence states of the catalysts. Fig. 4 displays the XPS spectra of Mn 2p, Cu 2p and O 1 s spectra for $Mn_3Al_1O_x$,

$Mn_2Cu_1Al_1O_x$ and Mn-Cu/γ-Al_2O_3 catalysts. The surface atom concentrations of Mn, Cu, and O at different oxidation states are summarized in Table 3. The Mn 2p spectra in Fig. 4a present two distinct peaks at around 642 and 653 eV, which can be ascribed to Mn $2p_{1/2}$ and Mn $2p_{3/2}$ spin-orbital peaks, respectively. By performing peak-fitting deconvolutions, the Mn $2p_{3/2}$ peak can be separated into three characteristic peaks which attributed to Mn^{2+} (640.9–641.1 eV), Mn^{3+} (642.0–642.4 eV) and Mn^{4+} (643.1–643.9 eV), indicating the Mn species exist in Mn^{2+}, Mn^{3+}, and Mn^{4+} states in the catalysts [8,26]. The Mn^{4+} binding energy in our study was higher than that observed from the pure bulk manganese oxide, which is related to the chemical
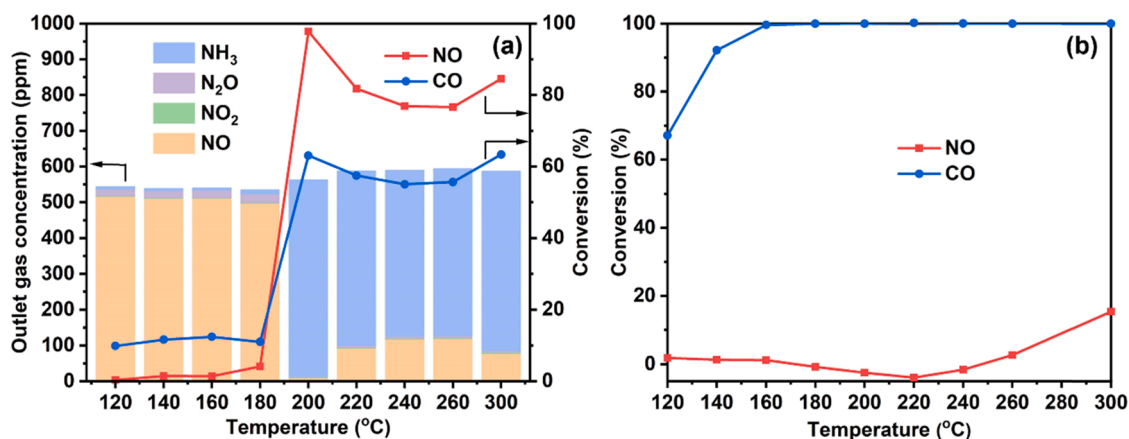
Fig. 3. The performance of $Mn_2Cu_1Al_1O_x$ catalysts for CO-SCR reaction in different atmosphere: (a) O_2-free, (b) O_2-rich. Reaction conditions: $[NO_x] = 500$ ppm, $[CO] = 5000$ ppm, $[O_2] = 5\%$ (when used), $[H_2O] = \sim 5\%$, balance Ar, total flow rate $= 200$ mL min^{-1}, operating temperature $= 120$–300 °C, catalyst 0.15 g.

Table 2

Mn, Cu, and Al content (wt%) and reaction rate (mmol m^{-2} h^{-1}) of NO_x and CO conversion for $Mn_2Cu_1Al_1O_x$, $Mn_3Al_1O_x$ and $Cu_3Al_1O_x$ catalysts.

Sample	Mn (wt%)[a]	Cu (wt%)[a]	Al (wt%)[a]	NO_x reaction rate $\times 10^{-3}$ (mmol m^{-2} h^{-1})				CO reaction rate $\times 10^{-2}$ (mmol m^{-2} h^{-1})			
				120 °C	140 °C	160 °C	180 °C	120 °C	140 °C	160 °C	180 °C
$Mn_2Cu_1Al_1O_x$	36.2	22.3	8.5	1.97	2.33	2.81	6.25	4.44	7.21	18.09	27.85
$Mn_3Al_1O_x$	58.2	–	9.2	7.37	10.50	15.67	18.80	0.10	0.20	0.39	0.72
$Cu_3Al_1O_x$	–	70.3	8.8	0.31	0.19	0.44	0.46	0.03	0.15	0.47	1.03

[a] Mn, Cu, and Al content (wt%) were measured by ICP-MS.

environment of Mn, including the amorphous manganese oxides and the interaction between manganese, aluminum and copper oxides, which was also reported by Kapteijn et. al [27]. Many previous studies have shown the NH₃-SCR activity is positively correlated with the content of Mn^{4+} at low temperatures [28,29]. The Mn^{4+}/Mn^{n+} ratio was calculated from the area ratio as 42.3% for $Mn_3Al_1O_x$, which is higher than that of $Mn_2Cu_1Al_1O_x$ (37.2%). After the addition of Cu, the Mn^{4+} content slightly decreased, accompanied by a certain decrease in NH₃-SCR activity at low temperatures. Mn-Cu/γ-Al_2O_3 showed the lowest Mn^{4+} content, corresponding to the lowest NH₃-SCR activity. These XPS data is consistent with the experimental activity tests (Fig. 2e).

As illustrated in Fig. 4b, the Cu 2p spectra for $Cu_3Al_1O_x$, $Mn_2Cu_1Al_1O_x$ and Mn-Cu/γ-Al_2O_3 catalysts exhibited several peaks corresponding to Cu $2p_{1/2}$, Cu $2p_{3/2}$ and shake-up satellites. The separated peaks at 933.9–934.2 eV as well as the shake-up satellites peaks at 940–948 eV confirmed the existence of Cu^{2+}, the peaks at 932.8–933.0 eV could be attributed to Cu^+. Besides, the XAFS technique was also employed to determine the chemical state of the doped Cu in $Mn_2Cu_1Al_1O_x$ catalysts. The pre-edge features of the normalized XANES spectra of Cu K-edge for $Mn_2Cu_1Al_1O_x$ and reference samples (Cu foil, CuO, Cu_2O) are shown in Fig. 4c. The XANES results demonstrated that the absorption edge of Cu K-edge for $Mn_2Cu_1Al_1O_x$ was located between those of Cu_2O and CuO, suggesting a copper valence between +1 and +2, consistent with the XPS results. The Fourier transformations (FTs) of the corresponding k^3-weighted Cu K-edge EXAFS spectra in Fig. 4d display a contribution of Cu–O at ~ 1.5 Å for $Mn_2Cu_1Al_1O_x$. It was evident that no Cu—Cu bond (located at ~ 2.5 Å) were detected in $Mn_2Cu_1Al_1O_x$, indicating the absence of the metallic Cu clusters. Previous investigation have shown both Cu^+ and Cu^{2+} can serve as active sites for CO oxidation reaction [13,30–32]. The formation of dominant active sites may be related to the preparation method, type of support and the pre-treatment conditions of Cu-based catalysts [32]. Although both Cu^+ and Cu^{2+} presented in $Mn_2Cu_1Al_1O_x$, the Cu^+–CO species of high reactivity observed from the in-situ DRIFTS (Fig. 6c, d) suggests Cu^+ served as an important

active site for CO oxidation, especially in the NH₃-NO-CO-O_2 system. The Cu^+ content in $Mn_2Cu_1Al_1O_x$ was higher than that in $Cu_3Al_1O_x$, which was due to the interaction between the Mn and Cu in the mixed oxides.

The XPS spectra of O 1s for these three catalysts are depicted in Fig. 4e. It is widely accepted that the O 1s spectra can be divided into two peaks. The peak located at the lower binding energy (~ 529.7 eV) was identified as the lattice oxygen (O_α) and the peak located at higher binding energy (~ 531.5 eV) was identified as the surface chemisorbed oxygen (O_β) [33,34]. Table 3 shows the proportion of O_β in $Mn_2Cu_1Al_1O_x$ is higher than that in others, which indicates more oxygen vacancies is formed in $Mn_2Cu_1Al_1O_x$ deduced by Cu doping. This is favorable for the CO oxidation reaction as well as the NH₃-SCR reaction due to the higher mobility and reactivity of O_β [29].

Fig. 4f shows the ESR analyses for $Mn_3Al_1O_x$, $Mn_2Cu_1Al_1O_x$, and Mn-Cu/γ-Al_2O_3 catalysts performed at room temperature. All three catalysts exhibited a symmetrical sharp isotropic signal at around $g = 2.003$, which can be ascribed as an electron trapped oxygen vacancy. $Mn_2Cu_1Al_1O_x$ catalyst showed the strongest signal intensity, indicating it possesses the highest oxygen vacancy concentration due to the abundant lattice defects caused by Cu doping.

O_2-TPD analyses were further performed in order to investigate the surface defects and lattice oxygen mobility of catalysts. As the temperature increases, the desorption behavior of oxygen species can be divided into the following stages: (1) 60–300 °C, physically adsorbed oxygen molecular (ads-O_2) and adsorbed oxygen species (O_2^- or O^-) which associated with oxygen vacancies, (2) 300–600 °C, lattice oxygen species (O^{2-}), and (3) > 600 °C, bulk lattice oxygen species [35]. As shown in Fig. 4g, $Mn_2Cu_1Al_1O_x$ presented a considerable desorption peak at temperature range of 100–300 °C, indicating abundant oxygen species (O_2^- and O^-) existed on the surface in comparison to $Mn_3Al_1O_x$. This is due to the presence of abundant oxygen vacancies caused by the lattice defects in $Mn_2Cu_1Al_1O_x$, which is consistent with the observations from XPS and ESR as stated above. Surface oxygen vacancy defects
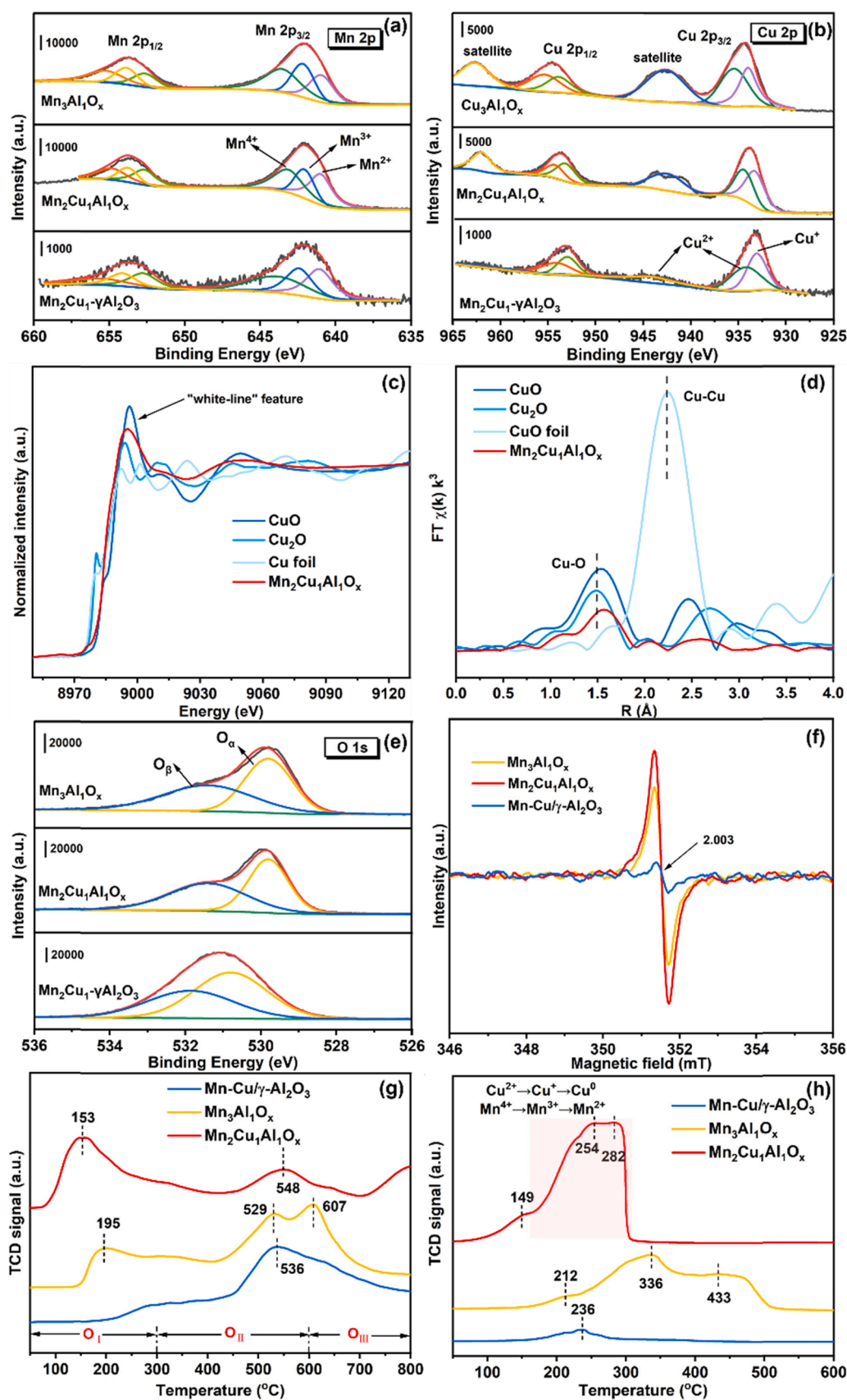
Fig. 4. XPS spectra of (a) Mn 2p and (b) Cu 2p, (c) normalized XANES spectra, (d) k^3-weighted Fourier transform spectra from EXAFS of Cu K-edge for Cu foil, Cu_2O, CuO and $Mn_2Cu_1Al_1O_x$ samples, (e) XPS spectra of O 1s, (f) ESR spectra, (g) O_2-TPD profiles, and (h) H_2-TPR profiles of $Mn_3Al_1O_x$, $Mn_2Cu_1Al_1O_x$, and Mn-Cu/γ-Al_2O_3 catalysts.

Table 3

The surface chemical components of $Mn_3Al_1O_x$, $Mn_2Cu_1Al_1O_x$, and Mn-Cu/γ-Al_2O_3 catalysts obtained by XPS analyses.

sample	$Mn^{4+}/(Mn^{4+} + Mn^{3+} + Mn^{2+})$(%)	$Cu^+/(Cu^{2+} + Cu^+)$(%)	$O_\beta/(O_\beta + O_\alpha)$ (%)
$Mn_3Al_1O_x$	42.3	–	49.5
$Cu_3Al_1O_x$	–	46.3	–
$Mn_2Cu_1Al_1O_x$	37.2	57.4	50.4
Mn-Cu/γ-Al_2O_3	33.0	42.5	41.5

are beneficial to the rapid replenishment of gaseous oxygen species and electron transfer during the chemical reactions process, especially in reactions involving O_2, and thus, further contributed to the higher reactivity of this catalyst [35–37]. Once the temperature reached above 450 °C, a large amount of oxygen species desorbed from Mn-Cu/γ-Al_2O_3 catalysts, suggesting there was only a small amount of adsorbed oxygen and the movable oxygen in Mn-Cu/γ-Al_2O_3 catalysts was mainly lattice oxygen which was much less active than adsorbed oxygen species.

The redox properties of catalysts are of great importance for both NH_3-SCR and CO oxidation reactions. To estimate the reducibility of $Mn_3Al_1O_x$, $Mn_2Cu_1Al_1O_x$, and Mn-Cu/γ-Al_2O_3 catalysts, H_2-TPR experiments were carried out. For Mn-based catalysts, the reduction of manganese oxides generally undergo the following continuous transformations: $MnO_2 \rightarrow Mn_2O_3 \rightarrow Mn_3O_4 \rightarrow MnO$ ($Mn^{4+} \rightarrow Mn^{3+} \rightarrow Mn^{2+}$) [35]. As shown in Fig. 4h, $Mn_3Al_1O_x$ catalyst exhibited two main reduction peaks at ~ 336 °C and ~ 443 °C, which could be attributed to the reduction processes of $Mn^{4+} \rightarrow Mn^{3+}$ and $Mn^{3+} \rightarrow Mn^{2+}$, respectively. The

overlapped peaks between 100 and 300 °C for $Mn_2Cu_1Al_1O_x$ catalysts were considered to be the reduction of the copper oxides and manganese species. The H_2 consumption of $Mn_3Al_1O_x$, $Mn_2Cu_1Al_1O_x$, and Mn-Cu/γ-Al_2O_3 was calculated as 2.37, 3.21, and 0.24 mmol g^{-1}, respectively, demonstrating that more reducible species were available in $Mn_2Cu_1Al_1O_x$. The larger amount of H_2 consumption as well as the shift of the reduction peak positions towards lower temperatures indicated the enhanced redox capability for $Mn_2Cu_1Al_1O_x$ catalysts. Two small shoulder peaks located at lower temperatures were also observed for $Mn_2Cu_1Al_1O_x$ (~ 149 °C) and $Mn_3Al_1O_x$ (~ 212 °C) catalysts. According to the literature reports, these peaks are predominantly related to the reduction of surface oxygen species [35,38]. Mn-Cu/γ-Al_2O_3 exhibited a very small reduction peak (~ 236 °C), indicating there were very few reducible species in this sample, which is consistent with its lowest catalytic activity.

In addition, both NH_3-TPD and CO-TPD experiments were conducted to investigate the adsorption behavior of reactants over synthesized catalysts (Fig. S4). Generally, NH_3 was adsorbed at the surface acidic sites on catalysts. Compared with Mn-Cu/γ-Al_2O_3, $Mn_2Cu_1Al_1O_x$ and $Mn_3Al_1O_x$ showed stronger acidity, leading to their superior deNO$_x$ performance (Fig. S4a). In CO-TPD experiments, during the entire desorption process, no CO but CO_2 was detected, which meant that CO strongly bound to surface oxygen and released in the form of CO_2 [39]. $Mn_2Cu_1Al_1O_x$ catalysts exhibited a broad CO_2 desorption peak at 50–300 °C, demonstrating that the formed carbonates were easily decomposed. $Mn_3Al_1O_x$ and Mn-Cu/γ-Al_2O_3 catalysts showed very small desorption peaks at 50–400 °C and 600–700 °C suggesting that less carbonates were formed on the catalyst surface and they were more
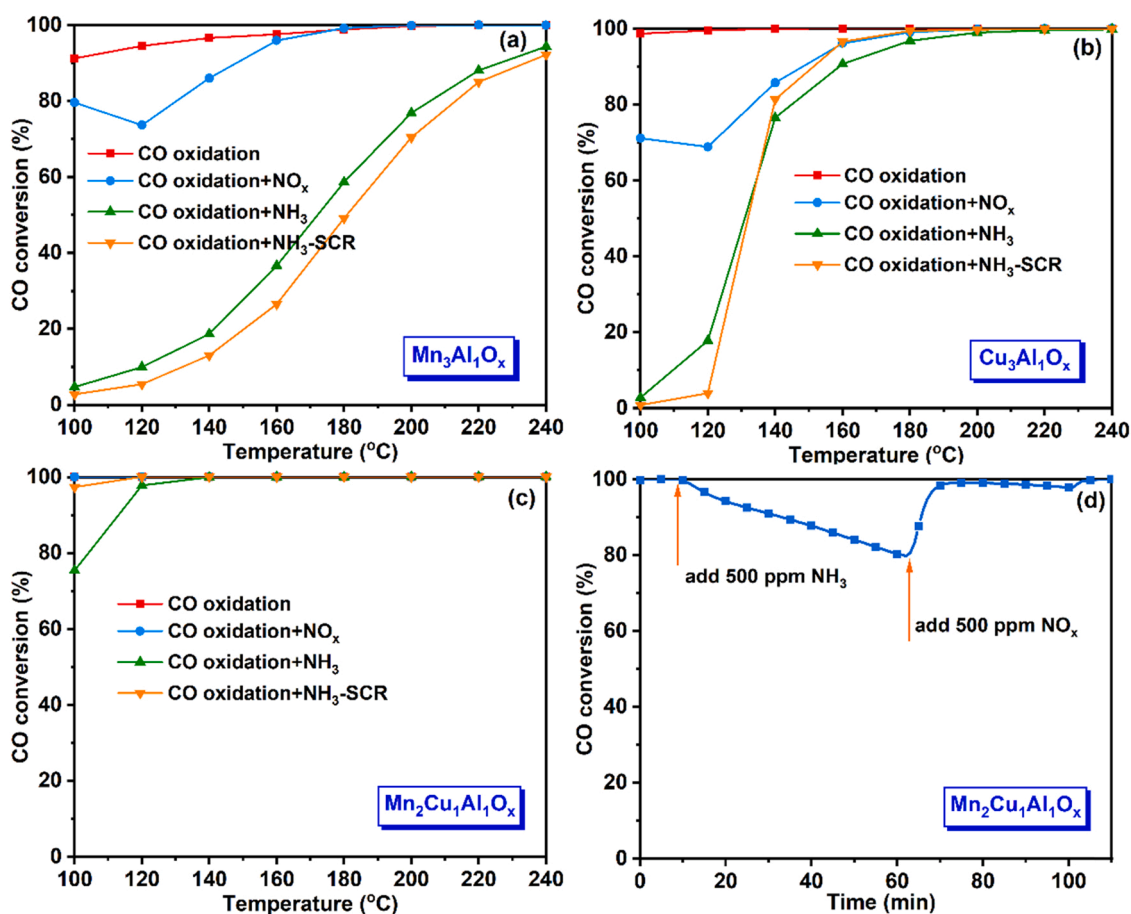
Fig. 5. Effect of different reaction conditions on CO oxidation over: (a) $Mn_3Al_1O_x$, (b) $Cu_3Al_1O_x$, (c) $Mn_2Cu_1Al_1O_x$, and (d) step response of the SCR atmosphere components over $Mn_2Cu_1Al_1O_x$ at 100 °C. Reaction conditions: [NO$_x$] = [NH$_3$] = 500 ppm (when used), [CO] = 5000 ppm. [O$_2$] = 5%, balance Ar, total flow rate = 200 mL min^{-1}, catalyst 0.15 g, all catalysts were pretreated in situ for 30 min in 5% O_2 (balance Ar) before each test.

stable, which was not conducive to CO oxidation.

3.4. Interaction principal between NH₃-SCR and CO oxidation reactions

The results in Section 3.2 revealed that there is interaction between NH_3-SCR and CO oxidation reactions, particularly the addition of NO_x and NH_3 inhibits the CO oxidation activity for $Cu_3Al_1O_x$. We are curious either it is NO_x or NH_3 actually effects the CO oxidation process. Therefore, the CO oxidation activities in the presence of NO_x (noted as CO oxidation + NO_x), in the presence of NH_3 (noted as CO oxidation + NH_3), and in the presence of both NO_x and NH_3 (noted as CO oxidation + NH_3-SCR) were comparatively evaluated over $Mn_3Al_1O_x$, $Cu_3Al_1O_x$, and $Mn_2Cu_1Al_1O_x$, respectively. Water vapor was removed in order to eliminate its interference with the other reactants.

Fig. 5a, b indicate the CO conversions over $Mn_3Al_1O_x$ and $Cu_3Al_1O_x$ catalysts can be inhibited by both NO_x and NH_3. By adding 500 ppm NO_x, the CO conversions were slightly decreased for certain extent, while adding 500 ppm NH_3 resulted in a much more significant influence on the CO conversion for both catalysts. Moreover, with the addition of both NO_x and NH_3, the resulting CO conversion profile is similar to that with only NH_3. Particularly at 100–120 °C, the CO conversions were significantly decreased from > 90% to lower than 20% by adding NH_3 and NO_x, or even only NH_3. Therefore, it is clear that NH_3 is the predominant inhibitor for CO oxidation over $Mn_3Al_1O_x$ and $Cu_3Al_1O_x$ catalysts.

Fig. 5c shows that over the $Mn_2Cu_1Al_1O_x$ catalyst, the inhibition effect by NH_3 is obviously weakened and the effect by NO_x is almost

disappeared. With 500 ppm NH_3, the CO conversion was only slightly effected at 100 °C. Interestingly, the CO conversion in the co-presence of NO_x and NH_3 was even higher than that with only NH_3, suggesting the CO-SCR reaction may occur to a certain degree and contribute to the CO conversion at low temperatures (100–120 °C).

To further confirm that NH_3 indeed has more severe influence on CO oxidation, a step response experiment was designed and performed at 100 °C, as shown in Fig. 5d. Initially the CO conversion was close to 100%, after adding 500 ppm NH_3, the CO conversion gradually decreased to 75.4% after 50 min. This indicates that NH_3 may compete the adsorption sites with CO on the surface of $Mn_2Cu_1Al_1O_x$ catalyst, leading to the decrease of CO conversion. Then with the addition of 500 ppm NO_x, the CO conversion was quickly recovered to 100%, which can be attributed to the consumption of adsorbed NH_3 by NO_x via NH_3-SCR reaction. These results revealed that the interaction principal between NH_3-SCR and CO oxidation reactions can be described by the competitive adsorption of NH_3 and CO, and the dynamic consumption of adsorbed NH_3 by NO_x, and the dynamic consumption of adsorbed CO by O_2. Since the O_2 concentration was high (5%), the contribution from CO-SCR reaction should be minor and only happened at low temperatures (100–120 °C).

3.5. In-situ DRIFTS studies

3.5.1. Reaction mechanisms of NH₃-SCR and CO oxidation

Firstly, the reaction process of NH_3-SCR over $Mn_2Cu_1Al_1O_x$ at 160 °C was investigated by in-situ DRIFTS studies. After fully adsorbing
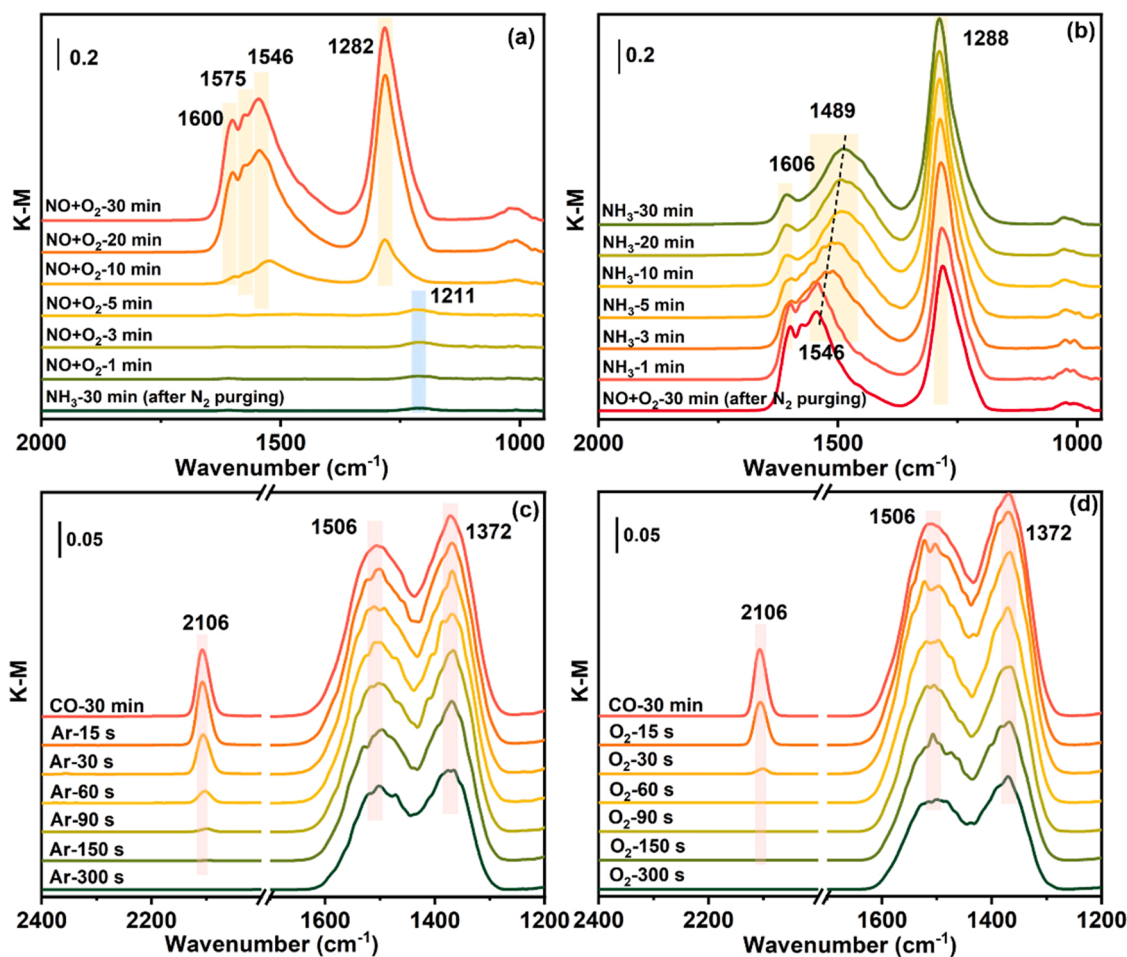
Fig. 6. In situ DRIFTS spectra of (a) passing NO + O_2 over NH_3 pre-adsorbed $Mn_2Cu_1Al_1O_x$ catalyst, (b) passing NH_3 over NO + O_2 pre-adsorbed $Mn_2Cu_1Al_1O_x$ catalyst, (c) passing Ar over CO pre-adsorbed $Mn_2Cu_1Al_1O_x$ catalyst, and (d) passing O_2 over CO pre-adsorbed $Mn_2Cu_1Al_1O_x$ catalyst at 160 °C. (Blue zone: NH_3 adsorbed species, pink zone: CO adsorbed species, yellow zone: NO_x adsorbed species.)

500 ppm NH_3 for 30 min, the peaks appeared at 1211 and 1607 cm^{-1} were attributed to the coordinated NH_3 on Lewis acid sites [26,40,41]. The bands at 3353, 3244, and 3160 cm^{-1} located at the NH stretching region also correspond to absorbed NH_3 (Fig. S5). Then after N_2 purging for 30 min, 500 ppm NO + 5% O_2 was inlet to react with the pre-adsorbed NH_3 species. As shown in Fig. 6a, the adsorbed NH_3 species vanished in 10 min, and the bands at 1600, 1575, 1546, and 1282 cm^{-1} of high strength formed with continuous NO + O_2 passing. According to the literature, the bands at 1575 and 1546 cm^{-1} can be assigned to bidentate nitrate species on manganese oxides, while the bands at 1282 cm^{-1} were attributed to monodentate nitrates [41]. The band at 1600 cm^{-1} can be ascribed to bridged nitrate [42]. Similarly, the reaction of 500 ppm NH_3 with pre-adsorbed NO_x was also investigated by in situ DRIFT under the same experimental condition. Fig. 6b indicates the adsorbed monodentate nitrate species (1288 cm^{-1}) did not react with NH_3, while the disappeared bridged nitrates indicated their reactivity with NH_3. The adsorption peak of bidentate nitrate shifted to a lower wavenumber (from 1546 to 1489 cm^{-1}) may imply the formation of another intermediate, such as nitrite species or ammonium nitrate [43, 44]. In addition, the in situ DRIFTS experiments upon 500 ppm NH_3 or 500 ppm NO + 5% O_2 adsorbed on $Mn_2Cu_1Al_1O_x$ catalysts at different temperatures (120, 160, 200 °C) were conducted to find out the relationship between adsorbed species and $deNO_x$ activity (Fig. S6). It is evident that the peaks ascribed to the coordinated NH_3 (bound to Lewis acids) were increased with the raising temperature, which is consistent with the increasing $deNO_x$ activity. While the adsorbed nitrate species did not accumulate with the raising temperature, except for the peaks at 1599 cm^{-1} (bridged nitrate). In all, we believe that both E-R and L-H mechanism coexist for the NH_3-SCR reaction over $Mn_2Cu_1Al_1O_x$ catalyst at 160 °C, but the E-R mechanism may dominant considering the positive dependence of the $deNO_x$ activity on catalyst acidity.

To verify the CO oxidation mechanism on $Mn_2Cu_1Al_1O_x$ catalyst, the in situ DRIFTS measurements for CO adsorption-desorption reaction were also conducted at 160 °C. The resulting spectra of $Mn_2Cu_1Al_1O_x$ adsorbing 5000 ppm CO for 30 min following by Ar and 5% O_2 purging are shown in Fig. 6c and d, respectively. The band at 2107 cm^{-1} after CO-adsorbing for 30 min was attributed to Cu^+–CO species (Fig. 6c) [45, 46]. Although the Cu^+–CO species were quite unstable which totally disappeared under Ar purging in 150 s, it disappeared more quickly under O_2 purging (60 s). This suggested that its disappearance was due to the reaction with O_2, rather than simply desorption under Ar purging [47]. The bands ascribed to carbonate species deduced by CO adsorption at 1506 and 1372 cm^{-1} decreased when being exposed to O_2 or Ar, indicating the decomposition of these carbonate species. It can be summarized that for CO oxidation proceeding on $Mn_2Cu_1Al_1O_x$, the high reactivity of Cu^+–CO species and the decomposition of the carbonate species derived from the CO adsorption both contribute to the production of CO_2.

3.5.2. Competitive adsorption of CO and NH_3

The competitive adsorption of CO and NH_3 over $Mn_3Al_1O_x$, $Cu_3Al_1O_x$ and $Mn_2Cu_1Al_1O_x$ was analyzed by in-situ DRIFTS measurements, respectively. The spectra were incessantly recorded with the gas mixture of 5000 ppm CO/500 ppm NH_3/Ar constantly flushing the surface of samples. For $Mn_3Al_1O_x$, the peaks appeared at 2175 and 2109 cm^{-1} were attributed to the gas CO adsorbed on the catalysts surface (Mn^{n+}–CO like species), which can be easily removed by purging argon (Figs. 7a, S7a) [48,49]. In addition, two peaks centered at 1602 and 1196 cm^{-1} can be assigned to the vibrations of C–O in carbonates species or the N–H in coordinated NH_3 (Lewis acid) [40,49]. The weaker band at 1443 cm^{-1} is assigned to the bidentate carbonate species or NH_4^+ ions (Brønsted acid) [41,48]. Since the location of the vibration peaks generated by the adsorption of NH_3 or CO were very similar to each other (Fig. S7a, b), it is difficult to distinguish the vibration peaks belongs to whether carbonate species or NH_3 adsorbed species. However, after the removal of NH_3, the intensity of the main peaks gradually decreased, suggesting
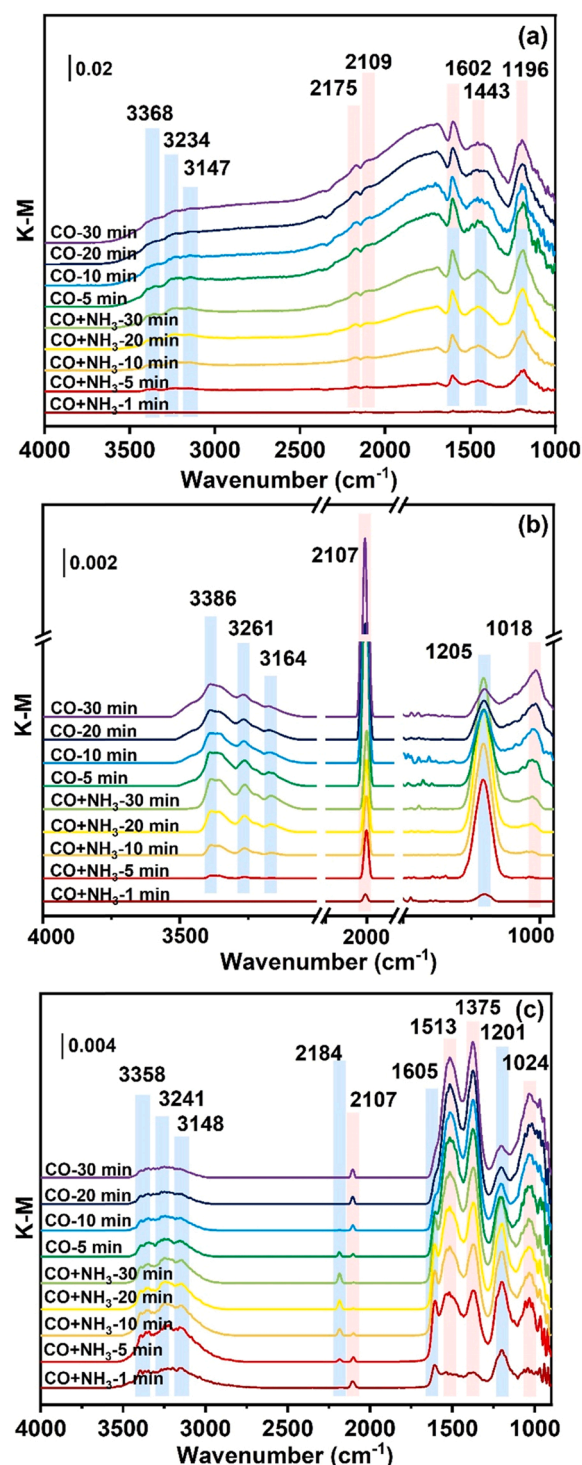
Fig. 7. In situ DRIFTS spectra of (a) $Cu_3Al_1O_x$, (b) $Mn_3Al_1O_x$, (c) $Mn_2Cu_1Al_1O_x$ catalysts collected at 160 °C under CO&NH_3 co-adsorption. (Blue zone: NH_3 adsorbed species, pink zone: CO adsorbed species.).

that the NH_3 adsorption declined. Several weak bands located at 3100–3400 cm^{-1} assigned to N–H vibration did not disappear even after removing NH_3 for 30 min, indicating that the species formed by NH_3 adsorption on the catalyst were very stable. Combined with the catalytic performance test results (Fig. 5a), it is reasonable to speculate that when CO and NH_3 coexist, the active sites of $Mn_3Al_1O_x$ catalyst were mainly occupied by NH_3, and thus CO oxidation was inhibited.

For $Cu_3Al_1O_x$, the sharp band at 2107 cm^{-1} was attributed to

Cu$^+$–CO, which was in line with literature studies (Fig. 7b) [45,46]. Besides, the characteristic peaks of coordinated NH$_3$ (3386, 3261, 3164 and 1205 cm^{-1}) existed throughout the whole experiment process [40]. Obviously, when NH$_3$ was removed, the peak at 2107 cm^{-1} grew rapidly. We can conclude that competitive adsorption exists between CO and NH$_3$ over Cu$_3$Al$_1$O$_x$, but the Cu$^+$–CO species (2107 cm^{-1}) are not completely suppressed, which allowed the better CO oxidation activity of Cu$_3$Al$_1$O$_x$ catalyst than that of Mn$_3$Al$_1$O$_x$ in the presence of NH$_3$

(Fig. 5a, b).

After the Mn$_2$Cu$_1$Al$_1$O$_x$ catalyst was exposed to the gas mixture of NH$_3$ and CO, vibration peaks formed by NH$_3$ and CO adsorptions were both detected (Fig. 7c). Interestingly, the peak at 2107 cm^{-1} (Cu$^+$–CO) was appeared at first 1 min, became weaker under the gas mixture flushing, and emerged again once the NH$_3$ was removed. This data indicates that the adsorption of CO on Cu$^+$ sites possesses faster kinetics while the adsorption of NH$_3$ on Cu$^+$ sites possesses higher binding
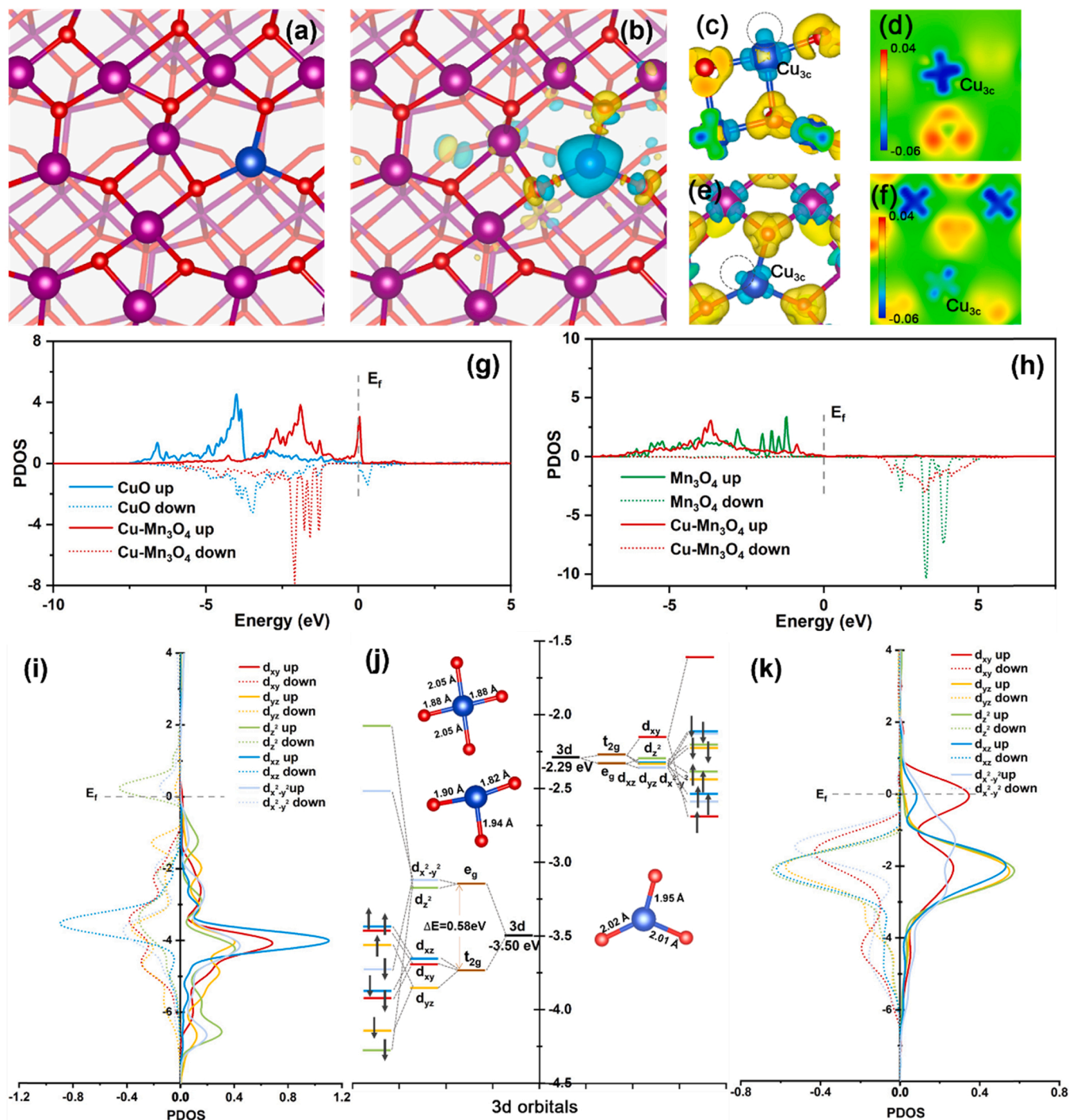
Fig. 8. (a) Optimized structures of Cu-Mn$_3$O$_4$(211) and (b) its secondary charge density differences. Charge density differences and corresponding 2D projections of (c, d) CuO(111) and (e, f) Cu-Mn$_3$O$_4$(211). Cyan area represents charge depletion, yellow area represents charge accumulation. PDOS comparison between the d band of (g) Cu$_{3c}$ atom of CuO(111) and Cu-Mn$_3$O$_4$(211) (the insert is the unoccupied 3d orbitals of Cu$_{3c}$ in Cu-Mn$_3$O$_4$(211) around Fermi level), (h) Mn$_{3c}$ atom of Mn$_3$O$_4$(211) and Cu-Mn$_3$O$_4$(211). 3d orbital-resolved DOS for Cu$_{3c}$ in (i) CuO(111), (k) Cu-Mn$_3$O$_4$(211), and (j) schematic band structure of Cu$_{3c}$, the left and right side of the vertical axis belong to CuO(111) and Cu-Mn$_3$O$_4$(211), respectively. (Color scheme: purple-Mn, blue-Cu, red-O).

strength on $Mn_2Cu_1Al_1O_x$. The competitive adsorption between NH_3 and CO is also highly dependent on their concentrations. Over $Mn_2Cu_1Al_1O_x$ catalyst, since the NH_3 could be quickly consumed on the active Mn^{n+} sites, the inhibitory effect by NH_3 on the CO adsorption on active Cu^+ sites was thus obviously weakened. This result explains why NH_3 has negligible influence on CO oxidation over $Mn_2Cu_1Al_1O_x$ catalyst, while such influence over neat $Cu_3Al_1O_x$ or $Mn_3Al_1O_x$ is much more severe.

3.6. DFT calculations

For deeply understanding the difference in the structure and activity between the catalysts contained single and dual active sites, DFT simulation was carried out. $CuO(111)$, $Mn_3O_4(211)$ and $Cu-Mn_3O_4(211)$ are selected as the calculation models of $Cu_3Al_1O_x$, $Mn_3Al_1O_x$, and $Mn_2Cu_1Al_1O_x$ catalysts, respectively. The top view and side view of optimized structures are displayed in Fig. S8. To investigate the charge distribution and transformation on the surface of catalysts, the charge density difference was plotted for $CuO(111)$, $Mn_3O_4(211)$, and Cu-

$Mn_3O_4(211)$ planes, respectively. The optimized structures of $Cu-Mn_3O_4(211)$ and its charge density differences are shown in Fig. 8a and b. The change transfer is clearly observed between Cu_{3c} and O atoms, and the induced unoccupied orbitals around the Cu atom will facilitate the interaction with adsorbate. Charge density differences and corresponding 2D projections of $CuO(111)$ and $Cu-Mn_3O_4(211)$ are shown in Fig. 8c–f. A large cyan area is observed at the top and center of Cu_{3c} sites, which is considered as the un-occupation orbit of Cu_{3c} species. Compared with original $CuO(111)$ and $Mn_3O_4(211)$ (Figs. 8c–f and S9a–d), the charge distribution of doped Cu_{3c} atom in $Cu-Mn_3O_4(211)$ is regulated, as well as Mn_{3c}, suggesting that the apparent electrons transfer between Cu and Mn atoms, which may provide the possibility for the reconstruction of the adsorption state of reactant molecules. Moreover, a little un-occupied orbit is observed over the surface of Cu_{3c} and Mn_{3c}, which is responsible for moderate Lewis acidity of $Mn_2Cu_1Al_1O_x$ catalyst [50]. This result agrees well with the in-situ DRIFTS data.

The fact which can not be ignored is that the shift of d band center for
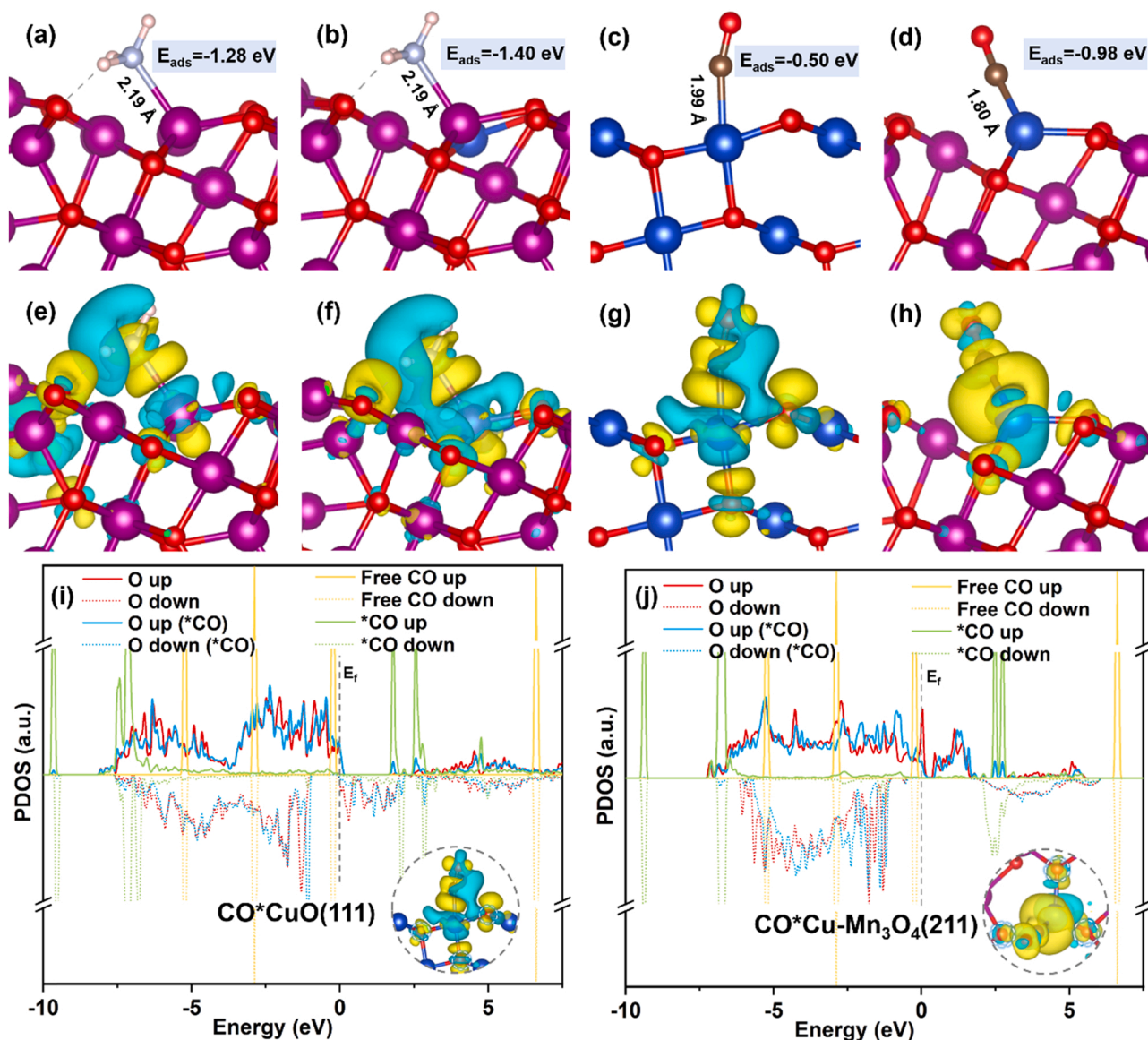
Fig. 9. Optimized structures, corresponding charge density differences and PDOS of (a, e) NH_3 adsorbed Mn_3O_4 (211), (b, f) NH_3 adsorbed $Cu-Mn_3O_4(211)$, (c, g) CO adsorbed $CuO(111)$ and (d, h) CO adsorbed $Cu-Mn_3O_4(211)$. The PDOS of CO molecule and coordinated O atoms with Cu_{3c} before and after CO adsorption: (i) CuO (111) and (j) Cu- $Mn_3O_4(211)$. * represents the adsorption state of CO, and the inset marks the coordinated oxygen atoms. Cyan area represents charge depletion, yellow area represents charge accumulation. (Color scheme: purple-Mn, blue-Cu, red-O, pink-H, silver-N, brown-C).

Cu_{3c} and Mn_{3c} atom which caused by the Cu doping effect. Fig. 8g, h display the projected density of states (PDOS) for d band of Cu_{3c} atom in CuO(111) and Cu-Mn_3O_4(211), Mn_{3c} atom in Mn_3O_4(211) and Cu-Mn_3O_4(211), respectively. The energy level of the d band center are listed in Table S2. D band center of Cu_{3c} atom doped in the Mn_3O_4 lattice obviously moves towards Fermi level from -3.50 eV to -2.29 eV, compared with that of the Cu_{3c} atom in CuO, which is more conducive to CO adsorption [51]. As shown in Fig. 8g, the 3d band of the Cu_{3c} in Cu-Mn_3O_4(211) is more localized and lies closer to Fermi level. Moreover, the appeared narrow 3d band across the Fermi level indicates a more active state of the doped Cu atom, which can promote electron transfer with adsorbed molecules. The 3d band of Mn_{3c} in Cu-Mn_3O_4(211) is more localized to some extent with the maintaining d band center, suggesting its less state change (Fig. 8h).

Subsequently, in order to investigate the shift of the Cu_{3c} d band in Cu-Mn_3O_4(211) towards Fermi level, schematic 3d orbital-resolved PDOS and energy order for Cu_{3c} in CuO(111) and Cu-Mn_3O_4(211) are depicted in Fig. 8i–k. Apparently, the energy level of the 3d band of Cu_{3c} in CuO(111) split into two energy levels, including t_{2g} orbital formed by downward-moving d_{xy}, d_{yz}, d_{xz}, and e_g orbital formed by upward-moving $d_{x^2-y^2}$, d_{z^2} (Figs. 8j, S10a). This energy redistribution eliminates the degeneracy and reduces the system symmetry and energy, which is exactly the Jahn-Teller effect [52]. The alteration in bond length caused by this effect is more pronounced for Cu_{4c} in bulk CuO, where two Cu—O bonds extended and two Cu—O bonds shrunk, in order to stabilize the system (Fig. S10b, c). In the case of Cu-Mn_3O_4(211), the Jahn-Teller effect of Cu_{3c} was significantly reduced, result in the shift of the d band center of Cu_{3c} towards Fermi level. The above comments explain the evolution of the d band center for the Cu_{3c} in Cu-Mn_3O_4(211) from the electronic level, which will eventually lead to the improved catalytic activity.

The adsorption energy of NH_3 and CO on the CuO(111), Mn_3O_4(211), Cu-Mn_3O_4(211) surface estimated by DFT calculation and the geometry optimized configurations are presented in Figs. 9a–h and S11. The adsorption of both NH_3 and CO molecules on the surface of catalysts are exothermic, which means the adsorption configurations are stable. The E_{ads} of NH_3 was higher than that of CO for all three models, indicating that NH_3 can be adsorbed more firmly on the active sites of the catalysts. The adsorbed NH_3 on the active sites (Mn_{3c} or Cu_{3c} atom) with N-end will further prevent the adsorption of CO, which leads to a suppressed CO conversion. This is consistent with the experimental results that the existence of NH_3 seriously affected the oxidation of CO under low temperatures (Fig. 5a, b).

As shown in Fig. 9a, b, NH_3 can strongly adsorb on Mn_{3c} sites of Mn_3O_4(211) and Cu-Mn_3O_4(211) with an adsorption energy of -1.28 eV and -1.40 eV, respectively, while it adsorbs on Cu_{3c} sites with an lower adsorption energy of -1.07 eV (Fig. S11a). From the charge density difference of NH_3 adsorbed on the surfaces in Figs. 9e, f and S11c, it can be seen that the charge transfer between N atom and Cu_{3c} site is less intensive than that on the Mn_{3c} site. Different from the NH_3 adsorbing on the CuO(111) surface, a hydrogen bond is additionally formed between an H atom of NH_3 and the O_{3c} site on the Mn_3O_4(211) and Cu-Mn_3O_4(211) surface, which will contribute to the adsorption and activation of NH_3 [53]. For Cu-Mn_3O_4(211), the adsorption of NH_3 also causes charge transfer on Cu_{3c}, indicating a synergistic effect between the doped Cu_{3c} and Mn_{3c} (Fig. S11e). DFT calculation and charge density difference analysis provide support to the superior NH_3-SCR activity over Mn_3O_4 and $Mn_2Cu_1O_x$ catalyst, which is related to the easier adsorption and activation of NH_3 on the catalysts.

For pure CO adsorption in Figs. 9c, d and S11b, CuO has a slight advantage compared to Mn_3O_4 in terms of adsorption energy (-0.42 eV on Mn_{3c} for Mn_3O_4(211) and -0.50 eV on Cu_{3c} for CuO(111)). Whereas for Cu-Mn_3O_4(211), the adsorption energy of CO on the surface Cu_{3c} site markedly increases to -0.98 eV, with a reduced bond length of 1.80 Å for Cu–C. From the charge density difference of the CO adsorbed on Cu_{3c} of CuO(111) and Cu-Mn_3O_4(211) in Fig. 9g, h, the bigger yellow area

between adsorbed CO and Cu_{3c} means more charge accumulation, implying stronger interaction between CO and Cu_{3c} on Cu-Mn_3O_4(211) surface, compared to that on CuO(111) surface. In addition, for CO adsorbed on CuO(111) surface, the cyan area appeared between the O atoms (adjacent to Cu_{3c}), CO molecular and Cu_{3c}, suggesting the charge transfer occurred between Cu_{3c}, CO molecular and O atom. Therefore, the PDOS of CO molecule and three O atoms coordinated with Cu_{3c} before and after CO adsorbed on CuO(111) and Cu-Mn_3O_4(211) are illustrated in Figs. 9i, j and S12. It can be seen that the PDOS of the three coordinated O atoms and CO exist a stronger resonance in CuO(111) after CO adsorbed, compared to that in Cu-Mn_3O_4(211). Further PDOS analysis of the p_x, p_y and p_z orbitals of the each coordinated O atom shows that the interaction between CO and each oxygen atom are different (Fig. S12). For example, the p_z orbital of atom 67 is affected more obviously, which can also be seen from the charge density difference diagram (Figs. 9g and S12a–c). The higher E_{ads} for CO on Cu-Mn_3O_4(211) indicates that Cu doping not only provides another active site for CO adsorption but also greatly enhances the interaction between CO and catalyst surface. On the other hand, although NH_3 may also be adsorbed on Cu_{3c}, the significant improvement in the adsorption energy of CO on Cu_{3c} is comparable to that of NH_3, which greatly enhances the competitive advantage of CO (Fig. S11 f,g). This is beneficial to CO oxidation particularly in the presence of competitive NH_3, in line with the experimental results (Fig. 5c). DFT calculations show that CO is more easily adsorbed on Cu site, while NH_3 is more inclined to adsorb on Mn site over Cu-Mn_3O_4(211), which enables both the NH_3-SCR and CO oxidation reactions to proceed simultaneously on one catalyst.

In view of the prominent strengthening of the CO adsorption on Cu_{3c} in Cu-Mn_3O_4(211), the different interactions of CO adsorbed on CuO (111) and Cu-Mn_3O_4(211) are further explained. The PDOS of 3d band of Cu_{3c} in CuO(111) and Cu-Mn_3O_4(211), 2p orbitals of the CO gas molecule, and their interaction are illustrated in Figs. 10 and S13. The α-spin 3d orbitals near the Fermi level of Cu_{3c} in Cu-Mn_3O_4(211) and 5σ orbitals of CO molecule are very close in energy, leading to partial occupation of the formed d-5σ orbitals. The inset in Fig. S13c also shows the corresponding p_z component in d-5σ orbitals. Moreover, the p_y component in the bonding orbitals (Fig. S13c) indicates that the $2\pi^*$ orbitals of the CO molecule also interact with d orbitals, forming a bonding orbitals and an anti-bonding orbitals. The electron donation of 5σ to 3d band and back donation of 3d band to $2\pi^*$ makes a stronger bonding of CO with Cu_{3c} [54]. While due to the strong Jahn-Teller effect of Cu_{3c} in CuO(111), the 3d band are not well matched with the 5σ orbital of CO, resulting in much weaker interaction between 3d band and 5σ orbitals. Different bonding conditions leads to the difference in the adsorption energy of CO between the two cases. The $4\sigma^*$, 1π and $2\pi^*$ of 2p orbitals interact weakly with the 3d band, causing some orbitals splitting. It can be concluded that Cu-doping strategy diminishes the Jahn-Teller effect of the Cu_{3c} atom to a great extent, which promotes CO adsorption on the Cu-Mn_3O_4(211) surface.

4. Conclusions

In this work, a bifunctional catalyst $Mn_2Cu_1Al_1O_x$ that possesses dual active sites and is highly active for both NH_3-SCR and CO oxidation reactions in the presence of excessive O_2 at low temperatures (180–220 °C) is designed for the first time. Compared with $Mn_3Al_1O_x$ and $Cu_3Al_1O_x$, $Mn_2Cu_1Al_1O_x$ showed higher specific surface area, excellent redox properties and abundant oxygen defects. In the NH_3-NO-CO-O_2 system, $Mn_3Al_1O_x$ was active for NH_3-SCR but poor for CO oxidation, and in contrast $Cu_3Al_1O_x$ was active for CO oxidation but poor for NH_3-SCR. However, under the same condition, the optimized $Mn_2Cu_1Al_1O_x$ catalyst achieved excellent catalytic performance for the simultaneous removal of NO_x and CO, with a conversion rate of 86.8% and 100% at 200 °C, respectively. The interaction principal between NH_3-SCR and CO oxidation reactions was carefully examined, which revealed that NH_3 was the predominant inhibitor for CO oxidation over
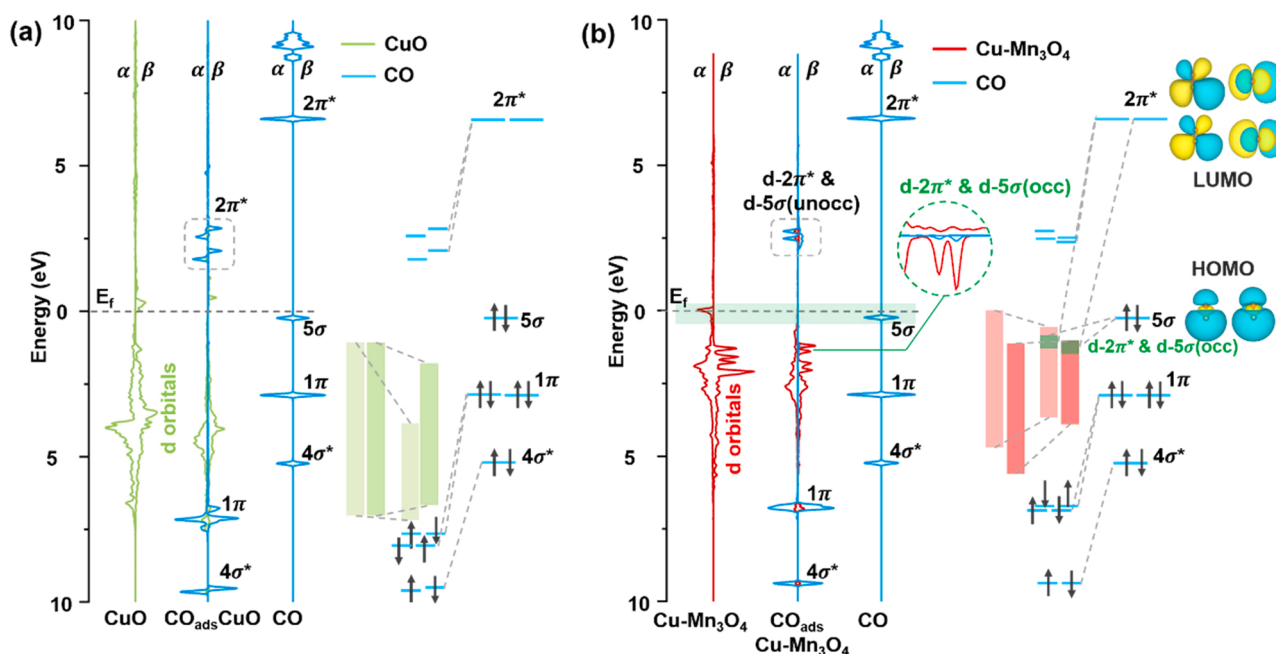
Fig. 10. (a) PDOS and schematic illustrations of 3d orbitals of CuO(111), 2p orbitals of the CO gas molecule, and their interaction. (b) PDOS for the Cu-Mn$_3$O$_4$(211) case. (α represents spin up and β represents spin down).

Mn$_3$Al$_1$O$_x$ and Cu$_3$Al$_1$O$_x$ catalysts. Over Mn$_2$Cu$_1$Al$_1$O$_x$ catalyst, the inhibition effect by NH$_3$ was obviously weakened due to the existence of dual active sites. In situ DRIFTS results also demonstrated the competitive adsorption of NH$_3$ and CO on the active sites. DFT calculation revealed the synergic effect between Cu and Mn atoms on the adsorption of NH$_3$ and CO, which can be attributed to the apparent electrons transfer. The adsorption energy results showed that CO was more easily adsorbed on Cu sites, while NH$_3$ was preferred to adsorb on Mn sites, enabling the simultaneous occurrence of both NH$_3$-SCR and CO oxidation reactions over one bifunctional catalyst Mn$_2$Cu$_1$Al$_1$O$_x$. The analysis of electronic structure revealed the difference of CO adsorption energy and bonding nature between CuO and Cu-Mn$_3$O$_4$ which caused by the Jahn-Teller effect.

CRediT authorship contribution statement

Rongrong Gui: Investigation, Writing – original draft, Validation, Data curation. **Jiewen Xiao:** Visualization, Data curation, Validation, Writing – original draft. **Yanshan Gao:** Writing – original draft, Formal analysis. **Yuran Li:** Methodology, Project administration. **Tingyu Zhu:** Validation, Resources, Project administration. **Qiang Wang:** Conceptualization, Data curation, Supervision, Resources, Project administration, Writing – review & editing.

Declaration of Competing Interest

The authors declare that they have no known competing financial interests or personal relationships that could have appeared to influence the work reported in this paper.

Acknowledgments

Appendix A. Supplementary material

Supplementary data associated with this article can be found in the online version at doi:10.1016/j.apcatb.2022.121104.

References

[1] K. Skalska, J.S. Miller, S. Ledakowicz, Trends in NO$_x$ abatement: a review, Sci. Total Environ. 408 (2010) 3976–3989.

[2] S.J. Tauster, L.L. Murrell, The NO-CO reaction in the presence of excess O$_2$ as catalyzed by iridium, J. Catal. 41 (1976) 192–195.

[3] A. Wang, L. Ma, Y. Cong, T. zhang, D. Liang, Unique properties of Ir/ZSM-5 catalyst for NO reduction with CO in the presence of excess oxygen, Appl. Catal. B Environ. 40 (2003) 319–329.

[4] T. Nanba, K. Wada, S. Masukawa, J. Uchisawa, A. Obuchi, Enhancement of activity of Ir catalysts for selective catalytic reduction of NO with CO by physical mixing with SiO$_2$, Appl. Catal. A Gen. 380 (2010) 66–71.

[5] Y.-W. You, Y.J. Kim, J.H. Lee, M.W. Arshad, S.K. Kim, S.M. Kim, H. Lee, L. T. Thompson, I. Heo, Unraveling the origin of extraordinary lean NO$_x$ reduction by CO over Ir-Ru bimetallic catalyst at low temperature, Appl. Catal. B Environ. 280 (2021) 119374–119386.

[6] Z. Li, H. Cheng, X. Zhang, M. Ji, S. Wang, S. Wang, The comparative study on the catalytic activity of Cu–M/Ce$_{0.8}$Zr$_{0.2}$O$_2$ (M = W, Nb, Cr and Mo) catalysts with dual-function for the simultaneous removal of NO and CO under oxygen-rich conditions, Catal. Sci. Technol. 11 (2021) 4987–4995.

[7] S. Xiong, Y. Peng, D. Wang, N. Huang, Q. Zhang, S. Yang, J. Chen, J. Li, The role of the Cu dopant on a Mn$_3$O$_4$ spinel SCR catalyst: improvement of low-temperature activity and sulfur resistance, Chem. Eng. J. 387 (2020) 124090–124101.

[8] Z. Wang, R. Guo, X. Shi, X. Liu, H. Qin, Y. Liu, C. Duan, D. Guo, W. Pan, The superior performance of CoMnO$_x$ catalyst with ball-flowerlike structure for low-temperature selective catalytic reduction of NO$_x$ by NH$_3$, Chem. Eng. J. 381 (2020) 122753–122762.

[9] Q. Wang, H. Xu, W. Huang, Z. Pan, H. Zhou, Metal organic frameworks-assisted fabrication of CuO/Cu$_2$O for enhanced selective catalytic reduction of NO$_x$ by NH$_3$ at low temperatures, J. Hazard. Mater. 364 (2019) 499–508.

[10] X. Yao, L. Chen, J. Cao, Y. Chen, M. Tian, F. Yang, J. Sun, C. Tang, L. Dong, Enhancing the deNO$_x$ performance of MnO/CeO$_2$-ZrO$_2$ nanorod catalyst for low-temperature NH$_3$-SCR by TiO$_2$ modification, Chem. Eng. J. 369 (2019) 46–56.

[11] S. Yang, C. Wang, J. Li, N. Yan, L. Ma, H. Chang, Low temperature selective catalytic reduction of NO with NH$_3$ over Mn–Fe spinel: performance, mechanism and kinetic study, Appl. Catal. B Environ. 110 (2011) 71–80.

[12] D.K. Pappas, T. Boningari, P. Boolchand, P.G. Smirniotis, Novel manganese oxide confined interweaved titania nanotubes for the low-temperature selective catalytic reduction (SCR) of NO$_x$ by NH$_3$, J. Catal. 334 (2016) 1–13.

[13] E.C. Njagi, C. Chen, H. Genuino, H. Galindo, H. Huang, S.L. Suib, Total oxidation of CO at ambient temperature using copper manganese oxide catalysts prepared by a redox method, Appl. Catal. B Environ. 99 (2010) 103–110.

[14] K.-J. Noh, K. Kim, H.J. Kim, D. Shin, J.W. Han, Improved CO oxidation via surface stabilization of ceria nanoparticles induced by rare-earth metal dopants, ACS Appl. Nano Mater. 2 (2019) 6473–6481.

[15] X. Xie, Y. Li, Z.Q. Liu, M. Haruta, W. Shen, Low-temperature oxidation of CO catalysed by Co_3O_4 nanorods, Nature 458 (2009) 746–749.

[16] M. Luo, J. Ma, J. Lu, Y. Song, Y. Wang, High-surface area CuO–CeO$_2$ catalysts prepared by a surfactant-templated method for low-temperature CO oxidation, J. Catal. 246 (2007) 52–59.

[17] C. Chen, M. Yang, Q. Wang, J.-C. Buffet, D. O'Hare, Synthesis and characterisation of aqueous miscible organic-layered double hydroxides, J. Mater. Chem. A 2 (2014) 15102–15110.

[18] J. Kuljiraseth, A. Wangriya, J.M.C. Malones, W. Klysubun, S. Jitkarnka, Synthesis and characterization of AMO LDH-derived mixed oxides with various Mg/Al ratios as acid–basic catalysts for esterification of benzoic acid with 2-ethylhexanol, Appl. Catal. B Environ. 243 (2019) 415–427.

[19] Q. Yan, Y. Gao, Y. Li, M.A. Vasiliades, S. Chen, C. Zhang, R. Gui, Q. Wang, T. Zhu, A.M. Efstathiou, Promotional effect of Ce doping in $Cu_4Al_1O_x$–LDO catalyst for low-T practical NH$_3$-SCR: steady-state and transient kinetics studies, Appl. Catal. B Environ. 255 (2019) 117749–117766.

[20] Q. Wang, D. O'Hare, Large-scale synthesis of highly dispersed layered double hydroxide powders containing delaminated single layer nanosheets, Chem. Commun. 49 (2013) 6301–6303.

[21] B. Ravel, M. Newville, ATHENA, ARTEMIS, HEPHAESTUS: data analysis for X-ray absorption spectroscopy using IFEFFIT, J. Synchrotron Radiat. 12 (2005) 537–541.

[22] C.I.N. Morgade, C.I. Vignatti, M.S. Avila, G.F. Cabeza, Theoretical and experimental analysis of the oxidation of CO on Pt catalysts supported on modified TiO$_2$(101), J. Mol. Catal. A Chem. 407 (2015) 102–112.

[23] A. Davó-Quiñonero, E. Bailón-García, S. López-Rodríguez, J. Juan-Juan, D. Lozano-Castelló, M. García-Melchor, F.C. Herrera, E. Pellegrin, C. Escudero, A. Bueno-López, Insights into the oxygen vacancy filling mechanism in CuO/CeO$_2$ catalysts: a key step toward high selectivity in preferential CO oxidation, ACS Catal. 10 (2020) 6532–6545.

[24] F. Cao, S. Su, J. Xiang, L. Sun, S. Hu, Q. Zhao, P. Wang, S. Lei, Density functional study of adsorption properties of NO and NH$_3$ over CuO/γ-Al$_2$O$_3$ catalyst, Appl. Surf. Sci. 261 (2012) 659–664.

[25] Q. Wang, Z. Wu, H.H. Tay, L. Chen, Y. Liu, J. Chang, Z. Zhong, J. Luo, A. Borgna, High temperature adsorption of CO$_2$ on Mg–Al hydrotalcite: effect of the charge compensating anions and the synthesis pH, Catal. Today 164 (2011) 198–203.

[26] Z. Fan, J.-W. Shi, C. Gao, G. Gao, B. Wang, C. Niu, Rationally designed porous MnO$_x$–FeO$_x$ nanoneedles for low-temperature selective catalytic reduction of NO$_x$ by NH$_3$, ACS Appl. Mater. Interfaces 9 (2017) 16117–16127.

[27] F. Kapteijn, A.D. van Langeveld, J.A. Moulijn, A. Andreini, M.A. Vuurman, A.M. Turek, J.M. Jehng, I.E.J. Wachs, Alumina-supported manganese oxide catalysts I. Characterization: effect of precursor and loading, J. Catal. 150 (1994) 94–104.

[28] B. Thirupathi, P.G. Smirniotis, Nickel-doped Mn/TiO$_2$ as an efficient catalyst for the low-temperature SCR of NO with NH$_3$: Catalytic evaluation and characterizations, J. Catal. 288 (2012) 74–83.

[29] L. Yan, Y. Gu, L. Han, P. Wang, H. Li, T. Yan, S. Kuboon, L. Shi, D. Zhang, Dual promotional effects of TiO$_2$-decorated acid-treated MnO$_x$ octahedral molecular sieve catalysts for alkali-resistant reduction of NO$_x$, ACS Appl. Mater. Interfaces 11 (2019) 11507–11517.

[30] W. Wang, P. Du, S. Zou, H. He, R. Wang, Z. Jin, S. Shi, Y. Huang, R. Si, Q. Song, C. Jia, C. Yan, Highly dispersed copper oxide clusters as active species in copper-ceria catalyst for preferential oxidation of carbon monoxide, ACS Catal. 5 (2015) 2088–2099.

[31] T. Huang, D. Tsai, CO oxidation behavior of copper and copper oxides, Catal. Lett. 87 (2003) 173–178.

[32] R.V. Goncalves, R. Wojcieszak, H. Wender, C.S.B. Dias, L.L.R. Vono, D. Eberhardt, S.R. Teixeira, L.M. Rossi, Easy access to metallic copper nanoparticles with high activity and stability for CO oxidation, ACS Appl. Mater. Interfaces 7 (2015) 7987–7994.

[33] H. Chang, X. Chen, J. Li, L. Ma, C. Wang, C. Liu, J.W. Schwank, J. Hao, Improvement of activity and SO$_2$ tolerance of Sn-modified MnO$_x$–CeO$_2$ catalysts for NH$_3$-SCR at low temperatures, Environ. Sci. Technol. 47 (2013) 5294–5301.

[34] L. Han, M. Gao, C. Feng, L. Shi, D. Zhang, Fe$_2$O$_3$-CeO$_2$@Al$_2$O$_3$ nano-arrays on Al-mesh as SO$_2$-tolerant monolith catalysts for NO$_x$ reduction by NH$_3$, Environ. Sci. Technol. 53 (2019) 5946–5956.

[35] S. Mo, Q. Zhang, J. Li, Y. Sun, Q. Ren, S. Zou, Q. Zhang, J. Lu, M. Fu, D. Mo, J. Wu, H. Huang, D. Ye, Highly efficient mesoporous MnO$_2$ catalysts for the total toluene oxidation: oxygen-vacancy defect engineering and involved intermediates using in situ DRIFTS, Appl. Catal. B Environ. 264 (2020) 118464–118479.

[36] S.B.T. Tran, H. Choi, S. Oh, J.Y. Park, Defective Nb$_2$O$_5$-supported Pt catalysts for CO oxidation: Promoting catalytic activity via oxygen vacancy engineering, J. Catal. 375 (2019) 124–134.

[37] Z. Su, W. Yang, C. Wang, S. Xiong, X. Cao, Y. Peng, W. Si, Y. Weng, M. Xue, J. Li, Roles of oxygen vacancies in the bulk and surface of CeO$_2$ for toluene catalytic combustion, Environ. Sci. Technol. 54 (2020) 12684–12692.

[38] Y. Luo, Y. Zheng, J. Zuo, X. Feng, X. Wang, T. Zhang, K. Zhang, L. Jiang, Insights into the high performance of Mn-Co oxides derived from metal-organic frameworks for total toluene oxidation, J. Hazard. Mater. 349 (2018) 119–127.

[39] F. Arena, R. Di Chio, L. Filiciotto, G. Trunfio, C. Espro, A. Palella, A. Patti, L. Spadaro, Probing the functionality of nanostructured MnCeO$_x$ catalysts in the carbon monoxide oxidation, Appl. Catal. B Environ. 218 (2017) 803–809.

[40] S. Ali, L. Chen, F. Yuan, R. Li, T. Zhang, S.u.H. Bakhtiar, X. Leng, X. Niu, Y. Zhu, Synergistic effect between copper and cerium on the performance of Cu$_x$-Ce$_{0.5−x}$-Zr$_{0.5}$ (x=0.1–0.5) oxides catalysts for selective catalytic reduction of NO with ammonia, Appl. Catal. B Environ. 210 (2017) 223–234.

[41] J. Liu, X. Li, Q. Zhao, J. Ke, H. Xiao, X. Lv, S. Liu, M. Tadé, S. Wang, Mechanistic investigation of the enhanced NH$_3$-SCR on cobalt-decorated Ce-Ti mixed oxide: in situ FTIR analysis for structure-activity correlation, Appl. Catal. B Environ. 200 (2017) 297–308.

[42] G. Zhou, P. Maitarad, P. Wang, L. Han, T. Yan, H. Li, J. Zhang, L. Shi, D. Zhang, Alkali-resistant NO$_x$ reduction over SCR catalysts via boosting NH$_3$ adsorption rates by in situ constructing the sacrificed sites, Environ. Sci. Technol. 54 (2020) 13314–13321.

[43] D. Wang, L. Zhang, K. Kamasamudram, W.S. Epling, In situ-DRIFTS study of selective catalytic reduction of NO$_x$ by NH$_3$ over Cu-exchanged SAPO-34, ACS Catal. 3 (2013) 871–881.

[44] L. Chen, Z. Si, X. Wu, D. Weng, DRIFT study of CuO-CeO$_2$-TiO$_2$ mixed oxides for NO$_x$ reduction with NH$_3$ at low temperatures, ACS Appl. Mater. Interfaces 6 (2014) 8134–8145.

[45] H. Wang, Z. Wang, J. Zhu, X. Li, B. Liu, F. Gao, L. Dong, Y. Chen, Influence of CO pretreatment on the activities of CuO/γ-Al$_2$O$_3$ catalysts in CO + O$_2$ reaction, Appl. Catal. B Environ. 79 (2008) 254–261.

[46] A. Davó-Quiñonero, M. Navlani-García, D. Lozano-Castelló, A. Bueno-López, J.A. Anderson, Role of hydroxyl groups in the preferential oxidation of CO over copper oxide–cerium oxide catalysts, ACS Catal. 6 (2016) 1723–1731.

[47] Y.A. May, S. Wei, W.Z. Yu, W.W. Wang, C.J. Jia, Highly efficient CuO/alpha-MnO$_2$ catalyst for low-temperature CO oxidation, Langmuir 36 (2020) 11196–11206.

[48] X. Zhang, Y. Deng, P. Tian, H. Shang, J. Xu, Y. Han, Dynamic active sites over binary oxide catalysts: In situ/operando spectroscopic study of low-temperature CO oxidation over MnO$_x$-CeO$_2$ catalysts, Appl. Catal. B Environ. 191 (2016) 179–191.

[49] R. Craciun, B. Nentwick, K. Hadjiivanov, H. Knözinger, Structure and redox properties of MnO$_x$/Yttrium-stabilized zirconia (YSZ) catalyst and its used in CO and CH$_4$ oxidation, Appl. Catal. A Gen. 243 (2003) 67–79.

[50] K. Alexopoulos, P. Hejduk, M. Witko, M. Reyniers, G.B. Marin, Theoretical study of the effect of (001) TiO$_2$ anatase support on V$_2$O$_5$, J. Phys. Chem. C 114 (2010) 3115–3130.

[51] M.T. Greiner, T.E. Jones, S. Beeg, L. Zwiener, M. Scherzer, F. Girgsdies, S. Piccinin, M. Armbruster, A. Knop-Gericke, R. Schlogl, Free-atom-like d states in single-atom alloy catalysts, Nat. Chem. 10 (2018) 1008–1015.

[52] S. Liu, B. Wang, X. Zhang, S. Zhao, Z. Zhang, H. Yu, Reviving the lithium-manganese-based layered oxide cathodes for lithium-ion batteries, Matter 4 (2021) 1511–1527.

[53] L. Han, M. Gao, J.-y. Hasegawa, S. Li, Y. Shen, H. Li, L. Shi, D. Zhang, SO$_2$-tolerant selective catalytic reduction of NO$_x$ over meso-TiO$_2$@Fe$_2$O$_3$@Al$_2$O$_3$ metal-based monolith catalysts, Environ. Sci. Technol. 53 (2019) 6462–6473.

[54] A. Soon, T. Söhnel, H. Idriss, Plane-wave pseudopotential density functional theory periodic slab calculations of CO adsorption on Cu$_2$O(111) surface, Surf. Sci. 579 (2005) 131–140.